Experimental Analysis of Wideband Spectrum Sensing Networks Using Massive MIMO Testbed

I. Dey, *Member, IEEE*, P. Salvo Rossi, *Senior Member, IEEE*, M. Majid Butt, *Senior Member, IEEE*, and Nicola Marchetti, *Senior Member, IEEE*

***Abstract*— In this paper, we investigate the practical implication of employing virtual massive multiple-input-multiple output (MIMO) based distributed decision fusion (DF) for collaborative wideband spectrum sensing (WSS) in a cognitive radio (CR)-like network. Towards that end, an indoor-only measurement campaign has been conducted to capture the propagation statistics of a 4×64 massive MIMO system with one authorized primary user (PU) and 4 unauthorized secondary users (SUs) transmitting simultaneously over a 20 MHz band divided into 1200 subcarriers. The frequency subcarriers belong to an Orthogonal-frequency-division-multiplexing (OFDM)-like set-up without the addition of cyclic prefix (CP) to the transmit symbols. Measurements are accumulated for different relative positions of the SUs which are analyzed to extract fading, shadowing, noise and interference power statistics. Log-likelihood ratio (LLR) based fusion rule and three different sets of sub-optimum fusion rules along with their time-reversed versions are formulated for combining decisions on the availability of each subcarrier transmitted by the SUs. The extracted channel characteristics are incorporated in both analytical and simulated performance analysis of the devised fusion rules for comparison and testing the validity of distributed DF in realistic collaborative WSS scenario.**

***Index Terms*— Wideband spectrum sensing, massive MIMO channel measurement, fading, shadowing and interference, fusion performance.**

I. Introduction

COGNITIVE Radio (CR) promises coherent and efficient sharing of available spectrum between authorized Primary Users (PU) and unauthorized Secondary Users (SUs). The SUs are accommodated on the same bandwidth as the PU only when the PU is inactive. A major challenge in implementing CR networks in densely deployed areas is the design of dynamic spectrum sensing and spectrum allocation algorithms for SUs without disturbing the existing PU. *Spectrum sensing* detects unused bandwidth portions dynamically without interfering with the activity pattern of the PU. Collaborative Wideband Spectrum Sensing (WSS) techniques accomplish the task of scanning multiple bands jointly or sequentially by exploiting spatial diversity and thereby improving the decision reliability on the availability of chunks of the spectrum [1], [2].

Distributed collaborative spectrum sensing performs better than the centralized option, especially in presence of fading and shadowing [3], [4]. It is to be mentioned here that collaborative spectrum sensing refers to a distributed sensing phase and centralized spectrum sensing alludes to a non-distributed processing phase. For distributed spectrum sensing, individual SU senses each of the available frequency bands and transmits its decision on the presence/absence of the PU on each of these bands to a Decision Fusion Center (DFC). The DFC implements array processing using different decision fusion rules through multiple antennas (small, moderate and large array) and combines all the SU decisions to arrive at the right one [5], [6]. However, all collaborative DF rules to date have only been proposed for narrowband spectrum sensing. As a consequence, their performance have only been evaluated in presence of Additive White Gaussian Noise (AWGN) and narrow-band fading over the propagation channel. Wideband channel impairments like frequency-selective fading, interference between closely-spaced frequency bands and fast large scale channel effects have never been considered when testing the effectiveness of the sensing and fusion algorithms.

Starting from the results in [6], in this paper, we consider a measurement campaign with small number of SUs transmitting their decisions on spectrum availability over interfering reporting channels. The appeal of the above setup has been recently confirmed experimentally through real measurement campaigns [7], [8]. We employ large number of receive antennas at the DFC, following the success observed in [9], [10] and thereby, mimicking a 'virtual massive MIMO communication scenario'. This follows from the idea that the advantages offered by massive MIMO will be really useful in the context of distributed decision making.

The decision transmitted from SUs on a group of closely-spaced frequency bands of interest (for e.g., Orthogonal Frequency Division Multiplexing (OFDM) based radio frequency (RF) communication system) will suffer from Inter-Symbol Interference (ISI), Inter-Carrier Interference (ICI) and Inter-Link Interference (ILI) during the reporting phase [11].

Manuscript received August 13, 2019; revised December 16, 2019 and April 4, 2020; accepted May 18, 2020. Date of publication May 29, 2020; date of current version September 16, 2020. This work was supported by EDGE through the Marie Skodowska-Curie COFUND Actions under Grant 13236/203377. The associate editor coordinating the review of this article and approving it for publication was W. Chen. *(Corresponding author: I. Dey.)*

I. Dey is with CONNECT, National University of Ireland, Maynooth, W23 F2K8 Ireland (e-mail: indrakshi.dey@mu.ie).

P. Salvo Rossi is with the Department of Electronic Systems, Norwegian University of Science and Technology (NTNU), 7491 Trondheim, Norway (e-mail: salvorossi@ieee.org).

M. Majid Butt is with Nokia Bell Labs, 91620 Nozay, France (e-mail: majid.butt@ieee.org).

Nicola Marchetti is with CONNECT, Trinity College Dublin, Dublin 2, D02 YY72 Ireland (e-mail: nicola.marchetti@tcd.ie).

Color versions of one or more of the figures in this article are available online at http://ieeexplore.ieee.org.

Digital Object Identifier 10.1109/TCOMM.2020.2998544

In such a scenario, the reliability of WSS can be improved by utilizing the correlation of cyclic prefix (CP) in multi-carrier signals. In order to take the advantage of both multi-carrier and massive MIMO technologies, combining them is a promising option. In that case, addition of CP reduces the available time for data transmission resulting in degradation of spectral efficiency in multi-user networks [12]. The possibility of eliminating (or shortening) CP lengths at the cost of additional ISI, ICI and ILI has been the focus of recent research in this area [13]. Though several interference cancellation techniques exist [14]–[16], the computation complexity increases exponentially when employed in conjunction with massive number of receive antennas.

If we want to apply the general framework of distributed DF to the OFDM-based collaborative WSS to address the major challenges in wideband CR networks, we have to rely on the assumption that number of antennas at the DFC is much larger than the number of transmitting SUs. In that case, we have to eliminate the use of CP in order to maintain high spectral efficiency in dense network scenarios. Rather, we have to depend on the large array gain of massive MIMO to average out the ISI, ICI and ILI introduced by the closely-spaced frequency bands in an OFDM-based system without CP. Moreover, to analyze the performance of OFDM-based WSS networks with collaborative DF, we have to characterize the propagation environment and the interfering components as the fusion rule statistics in many cases are proportional to channel coefficients (comprising of both large and small scale statistics) and are dependent on the instantaneous channel state information (CSI) [17], [18].

Despite the significance of the propagation statistics, no measurement campaigns have been performed specifically for evaluating WSS techniques for wideband CR networks over the years. The few that are conducted are generally modeling spectral occupancy [19], [20] or they are application specific [21] for spectrum detection and scanning techniques. To the best of our knowledge, there is no in-depth experimental investigation of the channel statistics (both small scale and large scale statistics) of the propagation channel and interference between competing SUs and DFC equipped with massive number of antennas that then incorporate them for performance evaluation of collaborative WSS techniques.

As massive MIMO systems are promised to be a part of future generations of telecommunication networks, a large number of measurement campaigns have been conducted to characterize the propagation channel. In recent years, the major focus has been system metrics for multi-user scenarios like spectral efficiency, capacity etc. [8], [22], [23], user separation and channel orthogonality [24], [25], propagation metrics over several frequency bands like pathloss, delay spread, coherence bandwidth [26] and root-mean-squared (rms) delay spread of the equivalent combined channel for linear precoding schemes [27]. Propagation environment characterization has also been the focus of [28] and [29] targeting 5G communication scenarios or [30], [31] for urban maro-cellular or micro-cellular environments. However, measurement campaign emulating wideband CR network-like scenario with distributed detection applied over large antenna array at the receiver has never been attempted before. Neither realistic propagation measurements have been incorporated to evaluate performance of fusion rules for collaborative WSS, especially in scenarios where the available frequency bands belong to a multi-carrier (OFDM-like) based RF communication system.

The primary contribution of this paper is two-fold. Firstly, we present a first-of-a-kind measurement campaign emulating a cognitive radio like network where several users (secondary) collaborate to take decision on the availability of the spectrum under the condition that the user (primary) licensed to use it is not communicating at all. The aim is to characterize the propagation environment between multiple SUs (each SU equipped with a single antenna) and DFC equipped with a large-size antenna array. The SUs jointly monitor multiple closely spaced frequency bands belonging to an OFDM-like set-up in absence of CP. In this study, we focus on ISI and ICI powers along with large and small scale channel statistics for each measurement route, location and spatial distribution of the transmit nodes. The channel statistics obtained are directly incorporated in both analytical and simulation based performance analysis of a large range of sub-optimum DF rules. We derive sub-optimum DF techniques with reduced complexity for the received signal at the DFC consisting of (i) Widely Linear (WL) rules, (ii) Standard Maximal Ratio Combining (MRC) and (iii) modified MRC (mMRC), generalizing to our setup those introduced in [32] for massive MIMO DF context. Towards this end, large-MIMO and wideband version of each fusion technique is developed.

Secondly, a new set of time-reversal (TR) based sub-optimum fusion rules; (iv) Time-Reversal WL (TR-WL), (v) Time-Reversal MRC (TR-MRC), and (vi) modified TR-MRC (TR-mMRC), are applied and analyzed to mitigate the additional interference incurred over closely spaced frequency bands due to removal of CP. For this set of DF rules, interference compensation is done through spatio-temporal focusing. The (TR-) WL and (TR-) MRC set of rules are particularly developed, as they are quite generic in nature and their performance do not necessarily vary a lot with the environments (indoor or outdoor). The MRC and mMRC do not require any assumption on the statistical distribution of the channel and the SU decision process (since they are ideally assumed to be error-free). On the other hand, WL set of rules depends on different reliabilities of the different SUs and takes into account the accuracy of the sensing process. Therefore performance analysis of (TR-) WL and (TR-) MRC set of rules will provide a clear picture of how distributed DF will perform in realistic collaborative WSS scenario.

The paper is organized as follows: Section II details the measurement set-up, scenario and the process by which information is extracted from the collected data. Section III provides results from analyzing the collected measurements. Section IV formulates different DF rules and compare their performance in realistic environment using the channel statistics derived from the measurement, while Section V concludes the paper.

[1]ILI is observed in outdoor scenarios, where the users are considerably far away from the Fusion Center (FC). Since we conduct our measurements in indoor scenario with only 4 SUs communicating simultaneously, we neglect presence of any ILI component.

Notations: Lower-case (resp. upper-case) bold letters denote vectors (resp. matrices), with a_k (resp. $a_{n,m}$) representing the kth element (resp. (n,m)th element) of $\mathbf{a}$ (resp. $\mathbf{A}$); $(\cdot)^t$ denotes transpose and $\mathbb{E}\{\cdot\}$, $\mathbb{V}\{\cdot\}$, $\mathbb{R}\{\cdot\}$, $\angle(\cdot)$, $(\cdot)^\dagger$, and $||\cdot||$ represents mean, variance, real-part, phase, conjugate transpose and Frobenius norm operators, respectively; $\mathbf{I}_N$ denotes the $N \times N$ identity matrix; $\mathbf{0}_N$ (resp. $\mathbf{1}_N$) denotes the null (resp. ones) vector of length N; $\underline{\mathbf{a}}$ (resp. $\underline{\mathbf{A}}$) denotes the augmented vector (resp. matrix) of $\mathbf{a}$ (resp. $\mathbf{A}$) i.e., $\underline{\mathbf{a}} \triangleq [\mathbf{a}^t \quad \mathbf{a}^\dagger]^t$ (resp. $\underline{\mathbf{A}} \triangleq [\mathbf{A}^t \quad \mathbf{A}^\dagger]^t$); $P(\cdot)$ and $p(\cdot)$ are used to denote probability mass functions (PMF) and probability density functions (PDF); $\mathcal{N}(\mu,\Sigma)$ and $\mathcal{N}_{\mathbb{C}}(\mu,\Sigma)$ denote normal distribution and circular symmetric complex normal distribution with mean vector μ and covariance matrix Σ respectively; $Q(\cdot)$ is used to denote the complementary cumulative distribution function (CCDF) of standard normal distribution; χ^2_k (resp. $\chi'^2_k(\xi)$) denotes a chi-square (resp. a non-central chi-square) distribution with k degrees of freedom (resp. and non-centrality parameter ξ) and 'mod L' refers to the modulo-operation which returns the remainder after division by L.

II. Measurement Campaign

A. Measurement Scenario

The time-varying channel impulse response (CIR) of 4×64 multiple-input-multiple-output (MIMO) channels with a center frequency of 2.45 GHz with 20 MHz bandwidth is recorded over this entire campaign. The room and the location of the transmitters are chosen such that they include both line-of-sight (LOS) and non-LOS (NLOS) communication paths, shadowing due to variety of electrical and laboratory equipments and pathloss due to building materials like dry-wall, glass, etc. The campaign is conducted in the circuits and antennas laboratory room located on the 5^{th} floor of the Elektro building at Norwegian University of Science and Technology (NTNU), Trondheim, Norway using the Re-configurable Radio Network Platform (ReRaNP). The room has dimensions of 9 meter(m) in length, 7m in width and 3m in height.

The measurement scenario considered in this paper is representative of a wide variety of environments. The SUs and the DFC are deployed within a single room, thereby replicating a high user-density situation; a scenario that will be encountered more frequently in near future with massive Internet-of-Things (IoT) networks in smart homes and smart building-like environments. The campaign is conducted in a laboratory room devoid of windows, but filled with different measuring equipments. Therefore, the measurement scenario also covers smart industry-like environment with several noisy electrical and automation equipments. The room is also a bit larger than a standard office room, thereby representing an open smart office-like environment, where several users, either stationary or with restricted movement, can access the network at the same time.

The transmit antennas are omni-directional rubber duck dipoles and are deployed simultaneously at a height of 1.3m at different locations of the room replicating an open laboratory environment. The receive antennas are set up with the radios on a metallic framework and are also omni-directional. Each measurement set is repeated for a stationary scenario and people moving around. In both cases, each measurement set is recorded for 10^7 snapshots, each snapshot being 5.5μs long. Therefore, each measurement set is recorded for an approximate total of 55 secs. Due to channel reciprocity conditions, it is assumed that channel estimates can be used for both uplink and downlink.

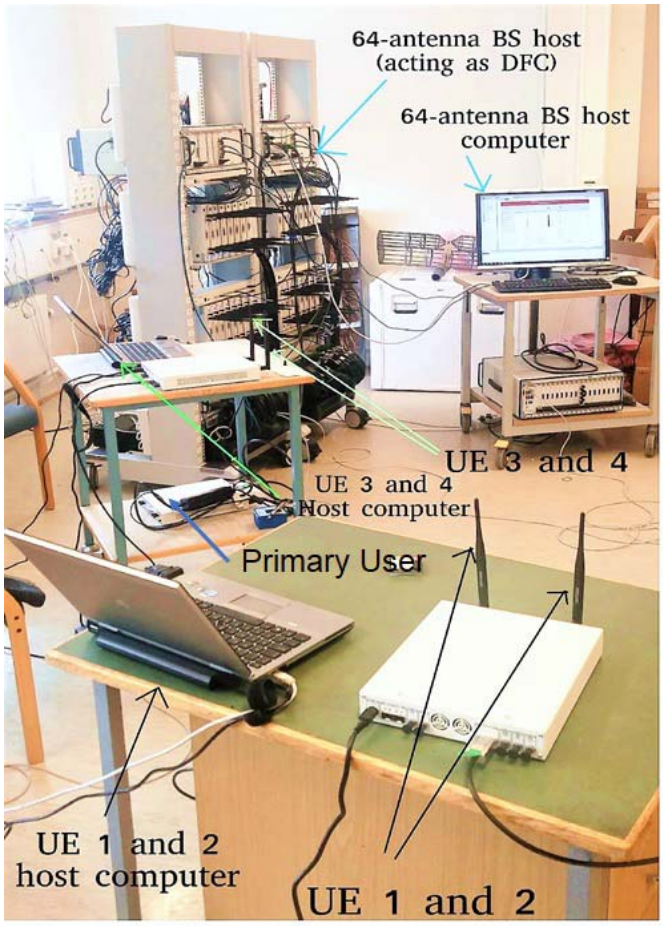

Fig. 1. Example of experiment set-up for $L7$ scenario of the indoor measurement campaign conducted in the circuits and antennas laboratory of NTNU, Norway.

The omni-directional transmit antennas are moved around the laboratory room at 8 different set of measurement locations. Among these locations, four sets ($L1$ - $L4$) have LOS conditions with two being obstructed LOS ($L3$, $L4$) due to presence of glass wall between the transmitters and the receivers. The rest of the four sets ($L5$ - $L8$) have NLOS propagation with two ($L5$, $L6$) being cases where the transmitters and receivers are separated by one and two sets of dry-walls respectively. An example scenario representing NLOS propagation condition i.e. $L7$ is shown in Fig. 1.

For propagation characterization, we consider a wideband collaborative spectrum sensing network with transmitters emulating secondary users (SU) ($K = 4$) who are looking to transmit on a frequency band if the primary user (PU) authorized to transmit on that band is silent. Therefore, we are emulating an uplink communication scenario, where the sensing information from the SUs on the different frequency bands are transmitted to a DFC equipped with multiple antennas (the number of antennas at the DFC is way more than the number of SUs).

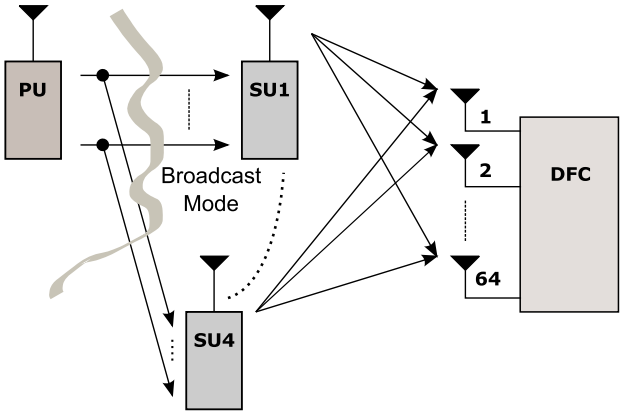

Fig. 2. System model for measured collaborative WSS network.

Let N denotes the total number of antennas at the DFC. For our measurement set-up, each SU is equipped with only one transmit antenna and $N = 64$. A system model is presented in Fig. 2 to depict the communication scenario.

Out of 8 different measurement scenarios, for the first two cases $L1$, $L2$ and the last two cases $L7$, $L8$, the four SUs are located close to each other with only 2-3m inter-spacing where signal separation is difficult. While for the other set of scenarios, $L3$, $L4$, $L5$ and $L6$, the users are far away from each other with more than 25 m of spacing and are separated by partitions like glass-wall and dry-walls. These set of scenarios represent condition, where good channel orthogonality is expected at the receiver station. Therefore, four different propagation conditions are investigated,

- Transmitting units close to each other at $L1$ and $L2$ having LOS path to the receiver station (hereafter we will refer to as 'Tx-cls-LOS')
- Transmitting units close to each other at $L7$ and $L8$ having NLOS path to the receiver station (hereafter referred to as 'Tx-cls-NLOS')
- Transmitting units far apart from each other at $L3$ and $L4$ having LOS path to the receiver station but separated by glass walls (hereafter we will indicate as 'Tx-far-LOS')
- Transmitting units far apart from each other at $L5$ and $L6$ having NLOS path to the receiver station but separated by set of dry-walls (further entitled as 'Tx-far-NLOS').

B. Measurement Set-Up

This subsection articulates the details of the ensemble of equipments used to conduct an indoor large-scale MIMO based measurement campaign. In this campaign, 4 single-antenna stationary transmitters deployed within the transmission power range of the base station (BS), are used to send their decisions regarding a certain phenomenon to the BS, which in this case acts as a DFC. The transmit units (SUs) are prototyped using the Universal Software Radio Peripheral (USRP) Re-configurable I/O (RIO) with an integrated Global Positioning System Disciplined Oscillator (GPSDO) and single-input-single-output (SISO) wireless capabilities.

Each USRP RIO represents two SU modules. The DFC is implemented using USRP-RIO equipped with 64 synchronized

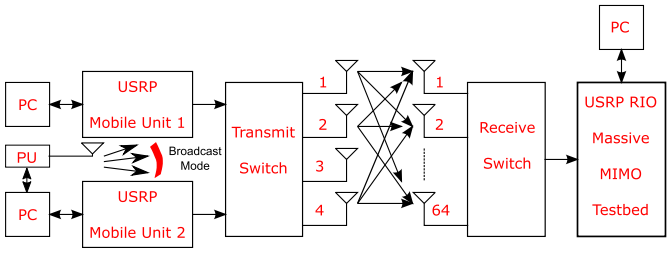

Fig. 3. Block diagram of measurement set-up.

omni-directional antenna ports forming a switched antenna array with 32 dual-polarized patches arranged with 32 elements in an equally spaced 4×8 rectangular configuration. The DFC consists of 2 units, each containing 32 radio chains by employing 16 National Instruments (NI) USRP-2943R devices. The framework implements a TDD system with an OFDM-like physical layer with 20 MHz bandwidth of operation. The DFC antenna array consists of wideband Long Periodic Dipole Arrays (LPDAs) with operating frequency ranging between 1.5 GHz and 6 GHz. The linearly polarized LPDA elements have half-power bandwidth of approximately 110° in the azimuth and 70° in the elevation giving a directive gain of 6dBi when used as a single element.

An overview of the measurement set-up is provided through the block diagram in Fig. 3. The 64 antenna MIMO testbed is controlled through a mounted PXI chassis and a PC center used for recording and conducting experiments. The system is designed with the LabVIEW Communication System Design Suite 2.0 running on USRP software defined radios (SDRs) allowing scaling from a 4-antenna upto an 128-antenna system. It is to be noted here that the antenna elements are placed 110 mm apart each with interleaved polarization orthogonal to its neighboring element thereby minimizing correlation between consecutive antenna elements. A common ground plane is placed behind the array elements which results in some variations in the directivity gain of the antenna elements.

Settings of two main files are configured for running the experiments: the mobile station (MS) host and the base station host. The base station host is meant to run on the unit controlling the 64-antenna set-up acting as DFC, where the mobile station should run on all the units emulating the SUs. The MIMO application framework does have functionality to calculate properties such as the impulse response, frequency response and power spectrum for the various channels between the BS and the MS, but said properties are only stored in a temporary data buffer for a few millisecond before they are discarded. Therefore, in order to save the data to some storage format, the BS and MS .gvi files are modified to continuously save various types of measurement samples to text files stored locally on the host computers.

Note on Software Modification

In order to implement the spectrum sensing framework within the measurement campaign set-up, the software files in the BS and MS configuration are modified to implement PU and SU functionalities. The host computer that controls the SUs, UE 3 and UE 4, is also programmed to control the SDR

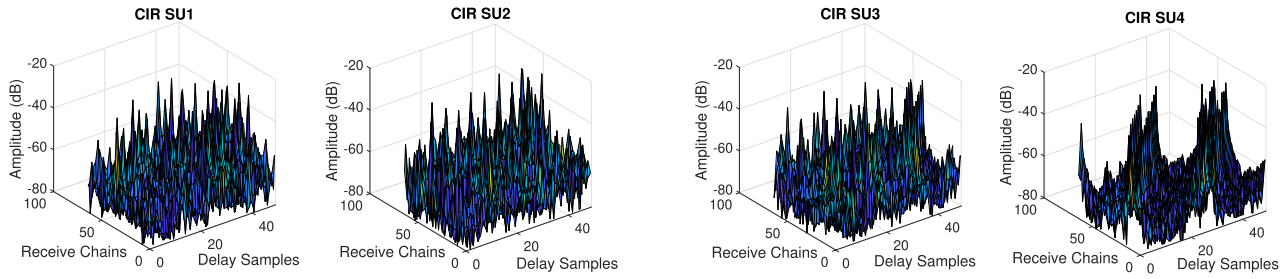

(a) CIR between SUs 1 and 2 and the DFC

(b) CIR between SUs 3 and 4 and the DFC

Fig. 4. CIRs observed at the DFC from each SU for measurement scenario $L5$ with people moving around in the measured indoor area.

acting as the PU. The PU implementation is designed in such a way that if the PU is silent, nothing is transmitted, whereas if active, a random bit sequence of 1s and 0s are created, then modulated with a BPSK modulation scheme at a carrier frequency specified by a control on the program panel, and finally broadcasted through the associated transmit antenna.

The carrier frequency is controlled using the program panel. It is varied between 2.44 and 2.46 GHz. However, the carrier frequency is kept fixed for each set of measurement. The SU implementation is designed to iteratively scan a certain spectrum region, each scan containing a center frequency and a certain bandwidth, where the entire spectrum is divided into several sub-carriers for the spectrum sensing network model presented in Section IV. For each scan, the power spectrum is computed and the peak power spectrum value is compared to a threshold value of -50 dB.

A value above the threshold means PU activity, where as a value below means that there is only noise present in the spectrum and therefore means no PU activity. When the Boolean PU lth sub-band activity indicator is switched on, the SUs are supposed to transmit a BPSK modulated symbol of $\{+1\}$ on the lth sub-band. When the PU is inactive, the SUs will transmit $\{-1\}$ on the lth sub-band. An overall 20 MHz band with center frequency of 2.45GHz is scanned for each measurement set and is divided into 1200 sub-carriers (i.e. $L = 1200$) with sub-carrier spacing of 15 KHz. Each of the single-antenna stationary SU transmits pilot symbols on all the 1200 sub-carriers during the channel estimate acquisition.

The SUs transmit their single-slot BPSK modulated local decisions $\{+1\}$ or $\{-1\}$ in parallel with the PU, only if the interference level between PU and SU transmissions is less than the maximum amount of interference tolerable by the PU. Such a technique follows the popular underlay configuration for CR networks [33] and assumes that the latency in the collection of all the SU decisions at the DFC does not grow with the total number of SUs in the network. If the PU is silent, there is no interference between the PU and the SUs. If the PU is active on the lth sub-band, SUs transmit their local decisions in parallel with the PU as long as the PU transmission achieves a target SINR of 30 dB.

C. Data Processing

The complex channel transfer function (CTF) coefficient $H^l_{n,k}$ over the lth sub-carrier between the kth SU and the nth antenna on the DFC is calculated by a minimum mean squared error (MMSE) estimate of the received signal with the known pilot symbols. The estimated CTF is denoted by $\tilde{H}^l_{n,k}$. The channel impulse response (CIR) between the kth SU and the receive set of antennas is obtained by taking inverse discrete Fourier transform (IDFT) of the CTF to obtain,

$$\tilde{h}^l_k(z) = \underset{l}{\text{IDFT}}\{\tilde{H}^l_{n,k}\} \tag{1}$$

where z is the delay bin with $Z = 10^7$ denoting the total number of delay bins or channel taps. Fig. 4 demonstrates an example set of CIRs for each SU observed at the DFC equipped with 64 receive antennas for dynamic measurement scenario at $L5$ over the sub-carrier band of 2449.97-2449.985 MHz (15KHz for each sub-carrier spacing).

The average received power from kth SU at location i is calculated as

$$P_{R,k}(i) = \frac{1}{N}\sum_n \sum_z |\tilde{h}^l_k(n,z)|^2 \tag{2}$$

and the average attenuation is given by,

$$A_k(i) = P_{R,k}(i)/(\alpha P_T) \tag{3}$$

with P_T as the transmit power and α as the additional losses to account for. If logarithm of distance is plotted against logarithm of $A_k(i)$, pathloss exponent (ν) can be determined from the slope of the best fit line to the log-log plot. The PDF of deviation of each $A_k(i)$ value from the best fit line to the log-log plot yields the shadowing distribution.

To analyze the small scale fading statistics, the power delay profile (PDP) of the channel is extracted by averaging the power along the n-axis to yield a Z-element vector for each SU. The average delay spread is the first moment of each SU induced PDP on the lth sub-carrier and is given by,

$$\overline{\tau}_{l,k} = \frac{\sum_z \tau_{l,k}(z)\left(\frac{1}{N}\sum_n |\tilde{h}^l_k(n,z)|^2\right)}{\sum_z \left(\frac{1}{N}\sum_n |\tilde{h}^l_k(n,z)|^2\right)} \tag{4}$$

The root-mean-squared (rms) delay spread is the square root of the second central moment of each PDP of each user channel on the lth sub-carrier given by,

$$\bar{\beta}^l_k = \sqrt{\overline{\tau}^2_{l,k} - (\overline{\tau}_{l,k})^2} \tag{5}$$

where

$$\overline{\tau}^2_{l,k} = \frac{\sum_z \tau^2_{l,k}(z)\left(\frac{1}{N}\sum_n |\tilde{h}^l_k{}^2(n,z)|^2\right)}{\sum_z \left(\frac{1}{N}\sum_n |\tilde{h}^l_k(n,z)|^2\right)}$$

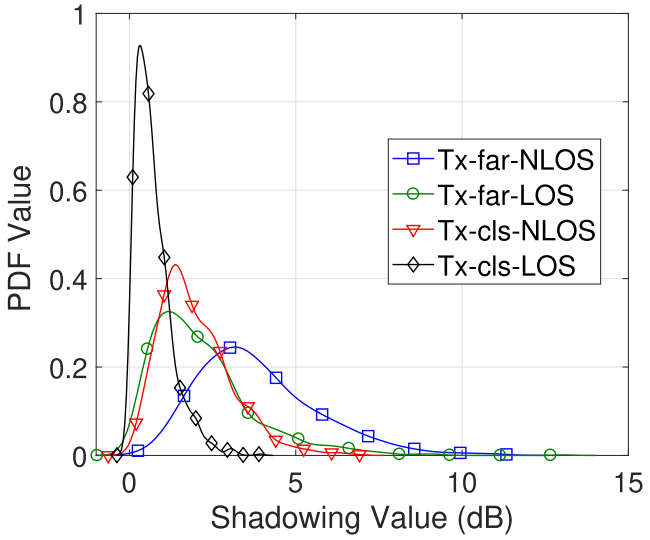

Fig. 5. Shadowing distributions for all environments.

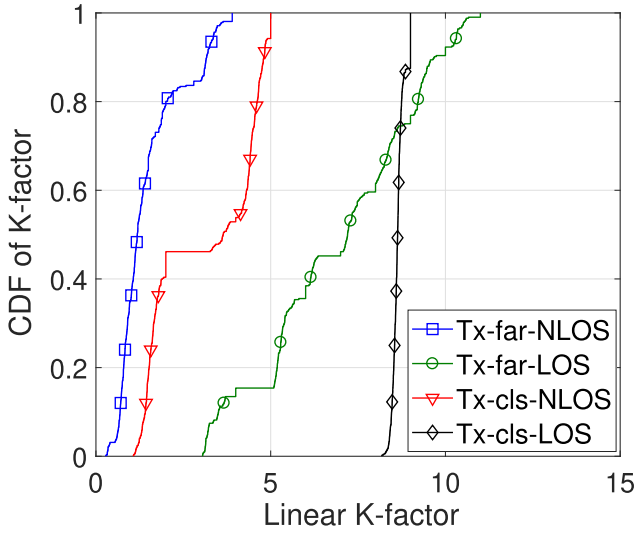

Fig. 6. CDF of K-factor for all environments.

TABLE I
LARGE SCALE PARAMETERS

Scenario	ν	$\mu_\lambda(dB)$	$\sigma_\lambda(dB)$
Tx-cls-LOS	2.51	-1.43	-4.9
Tx-cls-NLOS	2.37	3.01	0.57
Tx-far-LOS	2.93	3.42	3.54
Tx-far-NLOS	3.12	5.83	5.05

and the total PDP of each user channel on the lth sub-carrier is given by,

$$\mathcal{B}_k^l = \left(\tau_{l,k}(1)\left(\frac{1}{N}\sum_n |\tilde{h}_k^l(n,1)|^2\right), \ldots, \tau_{l,k}(Z)\left(\frac{1}{N}\sum_n |\tilde{h}_k^l(n,Z)|^2\right)\right)^t \quad (6)$$

The corresponding channel coherence bandwidth for each user antenna is calculated using $1/(5\bar{\beta}_k^l)$ [34].

III. MEASUREMENT RESULTS

A. Large Scale Channel Statistics

The shadowing distributions for LOS and NLOS scenarios are presented in Fig. 5. The pathloss exponents (ν) and mean and standard deviation (μ_λ, σ_λ) of the shadowing distributions are averaged over the measured sub-carriers and are summarized in Table I. Average values of μ_λ, σ_λ and ν are grouped by the type of measurement location and scenario. Shadowing distributions for all the measurement scenarios can be approximated using the Gamma distribution. The Pearson's chi-squared test [35] is used for verification of goodness of fit between Gamma and extracted shadowing distributions.

A very small variation in pathloss exponents is observed between different environments as the measurement campaign is executed in only one room and the distances between the SUs and the DFC are not varied much from one set of recordings to the other. However, as the inter-SU distances and the distances between the users and DFC increase, a large number of different shadowing values are encountered resulting in higher shadowing variance and increased shadowing severity.

B. Small Scale Channel Statistics

The small scale fading statistics is extracted from the estimated frequency domain response, $\tilde{\mathbf{H}}_k^l \in \mathbb{C}^{N\times Z}$, where $\tilde{H}_k^l(n,z)$ is the element on the nth row and zth column of $\tilde{\mathbf{H}}_k^l$. The number of frequency response values with independent small scale fading between the kth SU and the DFC is $R_k^l = \lfloor \Omega_{\text{Sig}}^l / \Omega_{\text{Coh},k}^l \rfloor$, where $\Omega_{\text{Coh},k}^l$ is the discrete coherence bandwidth of the kth user channel over the lth sub-carrier and Ω_{Sig}^l is the total discrete bandwidth of the measurement signal of the lth sub-carrier. For the kth SU, the fading vector can be defined by,

$$\vec{\xi_k^l} = [|\tilde{H}_k^l(0,0)|, \ldots, |\tilde{H}_k^l(N-1,0)|, |\tilde{H}_k^l(0,\Omega_{\text{Coh},k}^l)|, \ldots, |\tilde{H}_k^l(N-1, R_k^l\Omega_{\text{Coh},k}^l)|] \quad (7)$$

Chi-squared goodness-of-fit test is applied to each of the fading vectors, $\vec{\xi_k^l}$, for each SU against Rician distribution. A significance level of 5% [35] is used for verification of goodness of fit. Rician K-factor is estimated for all measurements satisfying the Chi-square test using the method of moments [36], the CDF plot of which is provided in Fig. 6. From the CDF plots of K-factors in Fig. 6, it is evident that lowest K-parameter is encountered if SUs are separated by partitions (glass or dry-walls) and no LOS paths exist between the SU and the DFC. Separation between the SUs leads to very low coordination between the users making the transmit signals vulnerable to noise, interference and fading.

Assuming the kth transmit antenna being visualized as a point-like source by the receive set of antennas, the steering vector from the kth antenna $\mathbf{U}(\phi_k^l)$ on the lth sub-carrier can be formulated using,

$$\mathbf{u}(\phi_k^l) = [1\; e^{j\pi\cos(\phi_k^l)}\; e^{j\pi 2\cos(\phi_k^l)} \ldots e^{j\pi(N-1)\cos(\phi_k^l)}] \quad (8)$$

where $\phi_k = \frac{1}{N}\sum_n\sum_z \angle\tilde{h}_k^l(n,z)$. Therefore for each measurement set, there will be K such steering vectors for lth sub-carrier given by, $\mathbf{U}(\Phi^l) = [\mathbf{u}(\phi_1^l), \mathbf{u}(\phi_2^l), \ldots, \mathbf{u}(\phi_K^l)]$, since each transmit antenna generates a separate steering vector over each sub-carrier.

TABLE II
OBSERVED RANGE OF VALUES FOR K-FACTORS

Scenario	K
Tx-cls-LOS	8 to 9
Tx-cls-NLOS	1.1 to 5
Tx-far-LOS	3 to 11
Tx-far-NLOS	0.75 to 4

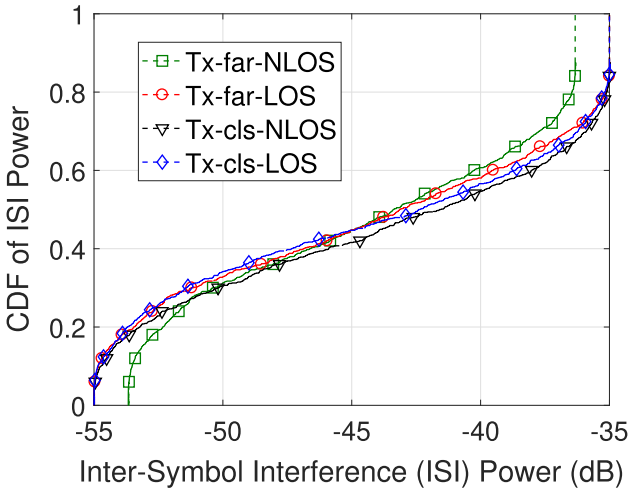

Fig. 7. CDF of ISI power for all environments.

TABLE III
RANGE OF VALUES FOR INTERFERING POWERS

Scenario	ISI Power (dB)	ICI Power (dB)
Tx-cls-LOS	-55 to -35	-60 to -50
Tx-cls-NLOS	-55 to -35	-74 to -36
Tx-far-LOS	-55 to -35	-66 to -44
Tx-far-NLOS	-54 to -36	-65 to -45

After extensive data fitting, it is possible to summarize and tabulate K-factors suitable for different indoor communication scenarios in large-scale MIMO-based spectrum sensing network. The ranges of K-factors for Rician distributed channels between the SUs and DFC are compiled in Table II.

C. Interference Analysis

The ReRaNP testbed operates on an OFDM like format, cyclic prefix (CP) has not been added to the sub-carriers. In that case, the channel between the SUs and the DFC will suffer from inter-symbol interference (ISI) and inter-carrier interference (ICI) which needs to be accounted for fusion performance analysis in Section IV. Finally Table III provides the range of values of ICI and ISI powers encountered for the four different measurement scenarios.

1) Inter-Symbol Interference (ISI): We calculate the ISI power within the lth sub-carrier after reception at the DFC using the average delay spread $\overline{\tau}_{l,k}$ of (4), given by,

$$\psi^2_{l,\text{ISI}} = \sum_{k=1}^{K} \overline{\tau}^2_{l,k} \tag{9}$$

for large number of receive antennas at the DFC, i.e. $N \to \infty$. The ISI power values for each sub-carrier are calculated for each measurement location and the CDF of the values for both LOS and NLOS scenarios are depicted in Fig. 7.

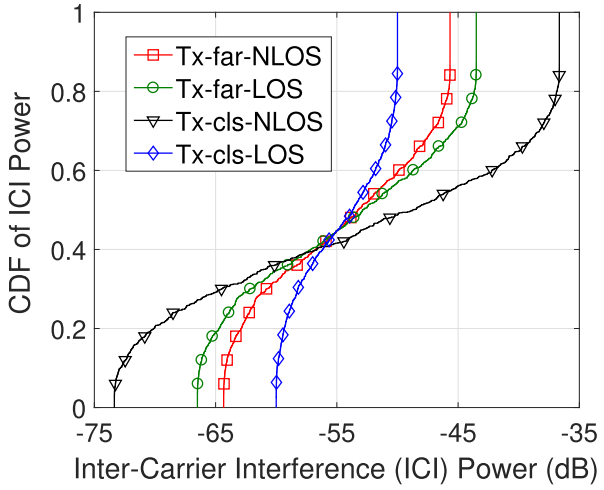

Fig. 8. CDF of ICI power for all environments.

TABLE IV
AVERAGE CHANNEL CAPACITY FOR DIFFERENT SCENARIOS

$\mathcal{C}$ (bps/Hz)	$L1$	$L2$	$L3$	$L4$	$L5$	$L6$	$L7$	$L8$
Low ρ^l	7.4	7.6	8.2	8.6	7.3	7.7	6.4	6.1
High ρ^l	10.7	10.1	11.4	11.9	14.8	14.3	12.8	12.3

2) Inter-Carrier Interference (ICI): Similarly, we calculate the ICI power from different neighboring sub-carriers on the lth sub-carrier after reception at the DFC using the mean-squared delay spread $\overline{\beta}^l_k$ of (5), given by,

$$\psi^2_{l,\text{ICI}} = \sum_{k=1}^{K} \sum_{q=1}^{L} |\overline{\beta}^q_k(d_{ql})|^2 \text{ for } q \neq l \tag{10}$$

for $N \to \infty$ referring to a large array of receive antennas at the DFC. The ICI power values are calculated from the qth sub-carrier on the lth sub-carrier and d_{ql} is the distance between the qth and lth sub-carriers ($= 15$ KHz between subsequent sub-carriers). The ICI power values for each sub-carrier are calculated for each measurement location and the CDF of the values for both LOS and NLOS scenarios are depicted in Fig. 8.

In order to visualize how the interference varies with transmit signal power and the location of the SUs in different parts of the indoor environment, Fig. 9 illustrate interfering powers as functions of transmit signal power. Interference power increases with the increase in transmit power and the inter-SU distances. As the end-to-end PDP decays, larger number of multipath components arrive at the receiver. The number of multipath components transferred to the DFC are more in case of NLOS propagation scenarios than the LOS scenarios. Thus the interfering power increases faster with the transmit signal power for the NLOS case than the LOS situation.

D. Achievable Channel Capacity

The average uplink channel capacity achievable on each sub-carrier (lth sub-carrier) can be calculated using,

$$\mathcal{C}^l = \frac{1}{Z} \sum_{z=1}^{Z} \log_2 \det \left(\mathbf{I}_K + \frac{\rho^l}{K} \tilde{H}^{l\dagger} \tilde{H}^l \right) \tag{11}$$

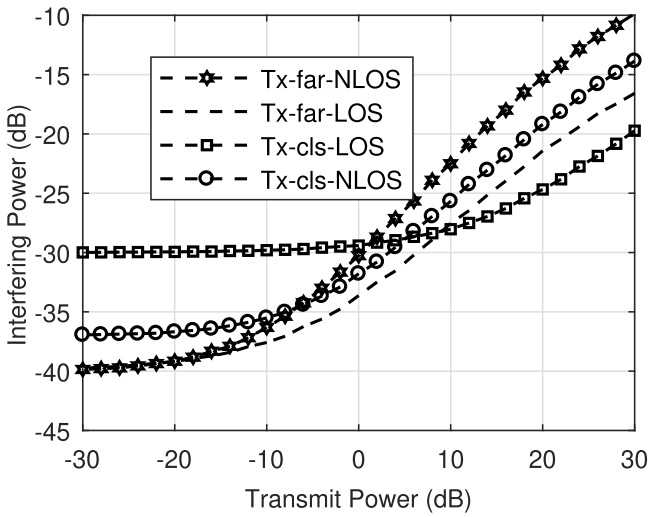

Fig. 9. Total power of the interfering components at the DFC as a function of the transmit signal power.

where ρ^l is the SINR on the lth sub-carrier. Average uplink capacity over the sub-carrier band of 2449.97-2449.985 MHz for each measurement scenario is tabulated in Table IV for high ($\rho^l = 2$ dB) and low ($\rho^l = 20$ dB) interference occurring cases. Achievable uplink capacity exhibit mixed results. Both in case of low and high SINR, higher capacity can be achieved when the SUs are far apart from each other. However, in case of low SINR, LOS communication scenario exhibit higher capacity than the NLOS case contrary to the observation for the high SINR cases.

IV. Wideband Collaborative Spectrum Sensing

A. System Description

In this paper, we consider an OFDM-based cognitive-radio like network with one PU and K unauthorized SUs finding opportunity to transmit in a licensed spectrum divided over L frequency sub-carriers, when the PU is inactive. Here, we will concentrate on the SUs transmitting their decisions on each sub-carrier, herein for the lth sub-carrier. Towards this end, we focus separately on sensing model of each SU and received signal model concerning the reporting phase at DFC.

1) Sensing and Local Decision Model: The kth SU ($k \in \mathcal{K} \triangleq \{1, 2, \ldots, K\}$), equipped with a single antenna, senses the L frequency bands and transmits its local (1-bit) decision on whether the PU is active or inactive in the lth sub-carrier. The local decision on lth frequency band is then mapped to a Binary Phase-Shift Keying (BPSK) modulated symbol, $x_k^l \in \mathcal{X} \triangleq \{+1, -1\}$ transmitted by the kth SU on the lth sub-carrier. Therefore, each SU transmits a total of L bits in each transmit symbol.

Let the hypothesis that the PU is active or silent on the lth frequency band be denoted by $\mathcal{H}_1^l$ (resp. $\mathcal{H}_0^l$) and is being transmitted on the lth sub-carrier. We assume that the local sensing and decision process at the kth SU over the lth sub-carrier is fully described by the conditional probabilities $P(x_k^l|\mathcal{H}_i^l)$. Specifically, we denote the probability of detection and false-alarm at kth SU on the lth sub-carrier as $P_{D,k}^l \triangleq P(x_k^l = 1|\mathcal{H}_1^l)$ and $P_{F,k}^l \triangleq P(x_k^l = 1|\mathcal{H}_0^l)$, respectively. Finally, for compactness, let $\mathbf{x}_k \triangleq \left[x_k^1 \cdots x_k^L\right]^t$ (resp. $\mathbf{x}^l \triangleq \left[x_1^l \cdots x_K^l\right]^t$) be the set of local decisions transmitted from kth SU on the L sub-carriers (resp. from all the K SUs on lth sub-carrier).

2) Signal Model: The DFC is equipped with N receive antennas over a wireless flat-fading multi-access channel; this set-up determines a distributed or 'virtual' massive MIMO channel. The N-length received vector at the DFC is denoted by $\mathbf{y}^l \triangleq \left(y_1^l, y_2^l, \ldots, y_N^l\right)^t$ where y_n^l is the signal received by the nth receive antenna on the lth sub-carrier. A large-array configuration is considered here, that is $N \gg K$ and the communication process on the reporting channel for the lth sub-carrier may be viewed as a $K \times N$ massive MIMO system.

The discrete-time signal model (after matched filtering and sampling) for the received signal at the DFC is given by,

$$\mathbf{y}^l = \sqrt{\rho^l}\mathbf{G}^l\mathbf{x}^l + \mathbf{w}^l + \mathbf{\Psi}^l \tag{12}$$

where $\mathbf{y}^l \in \mathbb{C}^N$, $\mathbf{G}^l \in \mathbb{C}^{N\times K}$, $\mathbf{x}^l \in \chi^K$, $\mathbf{w}^l \sim \mathcal{N}_{\mathbb{C}}(\mathbf{0}_N, \sigma_{w,l}^2\mathbf{I}_N)$ and $\mathbf{\Psi}^l \sim \mathcal{N}_{\mathbb{C}}(\mathbf{0}_N, \psi_l^2\mathbf{I}_N)$ are the received signal vector, the channel matrix, the transmitted signal vector, the noise vector and the interfering signal vector respectively. In (12), the constant ρ^l denotes the energy spent by any of the SUs during the reporting phase. The component for interference $\mathbf{\Psi}^l$ in (12) arises from the combination of ISI among symbols carrying decisions of all K SUs on each sub-carrier, and ICI due to nearby sub-carriers, and is given by $\psi_l^2 = \psi_{l,\text{ICI}}^2 + \psi_{l,\text{ISI}}^2$.

3) Channel Model: The channel coefficient vector $\mathbf{g}_{n,k}^l$ can be expressed as, $\mathbf{g}_{n,k}^l = \sqrt{\lambda_k}\mathbf{h}_{n,k}^l$ for $(n = 1, 2, \ldots N, l = 1, 2, \ldots L)$, where λ_k accounts for pathloss and shadowing experienced by the kth SU and remains constant over n and l. Each of the CIRs, $\mathbf{h}_{n,k}^l$ can in turn be modeled as linear time-invariant finite impulse response (FIR) filters with the order of Z, i.e., $\mathbf{h}_{n,k}^l = \left(h_{n,k}^l(0), \ldots, h_{n,k}^l(Z-1)\right)^t$ and $\mathbf{h}_{n,k}^l \sim \mathcal{N}_{\mathbb{C}}(0, \text{diag}(\mathcal{B}_k^l))$ where the vector $\mathcal{B}_k^l = \left(\beta_k^l(0), \ldots, \beta_k^l(Z-1)\right)^t$ is the PDP. Therefore, we have, $\mathbf{G}^l = \mathbf{H}^l\sqrt{\mathbf{D}}$ $(l = 1, 2, \ldots, L)$ where, $\mathbf{H}^l \in \mathbb{C}^{N\times K}$ denotes the matrix of the fast-fading coefficients and $\mathbf{D} \in \mathbb{C}^{K\times K}$ is a diagonal matrix where $d_{k,k} = \lambda_k$.

The fading vector of the kth SU can be given by,

$$\mathbf{h}_k^{\text{Rice},l} = \kappa_k^l\mathbf{u}(\phi_k^l) + \sqrt{1 - \kappa_k^{l\,2}}\;\hat{\mathbf{h}}_k^l \tag{13}$$

filling the kth column of $\mathbf{H}^l$. If $\mathbf{u}^l(\cdot)$ denotes the steering vector with $\hat{\mathbf{h}}_k^l \sim \mathcal{N}_C\left(\mathbf{0}_N, \mathbf{I}_N\right)$ characterizing the NLOS (scattered) component, $\kappa_k^l \triangleq \sqrt{\frac{K_k^l}{1+K_k^l}}$, where K_k^l is the Rician K-factor between kth SU and DFC on the lth sub-carrier.

4) Modified System Model: Here we develop the time-reversed (TR) version of the channel model in order to formulate the TR-based fusion rules. Let us denote the TR variant of the channel matrix on the lth sub-carrier as $\breve{\mathbf{G}}^l$. Each element of $\breve{\mathbf{G}}^l$ in this case can be expressed as, $\breve{\mathbf{g}}_{n,k}^l = \sqrt{\lambda_k}\breve{\mathbf{h}}_{n,k}^l$ for $(n = 1, \ldots, N,\ l = 1, \ldots, L)$, where $\breve{\mathbf{h}}_{n,k}^l$ is the TR version of $\mathbf{h}_{n,k}^l$, given by, $\breve{\mathbf{h}}_{n,k}^l = (h_{n,k}^l(Z-1), \ldots, h_{n,k}^l(0))^t$. Essentially, $\breve{\mathbf{h}}_{n,k}^l$ becomes $\breve{\mathbf{h}}_{n,k}^l \sim \mathcal{N}_{\mathbb{C}}(0, \text{diag}(\breve{\mathcal{B}}_k^l))$, where

$\breve{\mathcal{B}}_k^l = [\beta_k^l(Z-1), \beta_k^l(Z-2), \ldots, \beta_k^l(0)]$ is the TR version of the channel PDP and $\sum_{z=0}^{Z-1} \beta_k^l(z) = 1$. Based on these assumptions, we have $\breve{\mathbf{G}}^l = \breve{\mathbf{H}}^l\sqrt{\mathbf{D}}$ where $\breve{\mathbf{H}}^l$ denotes the TR channel matrix containing the fading coefficients.

Since, we are assuming favorable propagation condition, the channel matrices $\mathbf{G}^l$ are pairwisely orthogonal. Hence their time-reversed versions are also pairwisely orthogonal to each other and therefore, we can write, $\frac{1}{N}(\breve{\mathbf{G}}^l)^\dagger\breve{\mathbf{G}}^l \approx \breve{\mathbf{A}}^l$. In this case, $\breve{\mathbf{A}}^l = \mathbf{D} * [\text{diag}(\breve{\mathcal{B}}_k^l)]$. At the same time, the channel matrix will also be pairwisely orthogonal to its time-reversed version. Hence, as $N \to \infty$, $(\breve{\mathbf{G}}^l)^\dagger\mathbf{G}^l \approx \frac{1}{N}\mathbf{F}^l$. In this case, $\mathbf{F}^l = \left(\sqrt{\mathbf{D}} * \left[\text{diag}(\sqrt{\breve{\mathcal{B}}_k^l})\right]\right)^\dagger * \left(\sqrt{\mathbf{D}} * \left[\text{diag}(\sqrt{\mathcal{B}_k^l})\right]\right)$.

5) Performance Measures: We also assume that the SUs are located in a circular area around the DFC with radius $r_{\max} = 9$ m uniformly distributed at random and we assume that none of the SUs is closer to the DFC than $r_{\min} = 2$ m. The large-scale shadowing is characterized using $\lambda_k = \zeta_k(\frac{r_{\min}}{r_k})^\nu$, where ζ_k is a Gamma distributed random variable i.e. $\zeta_k \sim \mathcal{N}(2\mu_\lambda, \sigma_\lambda^2/2)$, where μ_λ and σ_λ are the mean and standard deviation in dB respectively. Also, r_k is the distance between the kth SU and the DFC and ν denotes the path-loss exponent (ν remains constant for all SUs over all the sub-carriers). The noise vector is generated according to $\mathbf{w}^l \sim \mathcal{N}_\mathbb{C}(\mathbf{0}_N, \sigma_{w,l}^2\mathbf{I}_N)$, where $\sigma_{w,l}^2$ is the noise spectral density over the lth sub-carrier. The interference vector is formulated according to $\mathbf{\Psi}^l \sim \mathcal{N}_\mathbb{C}(\mathbf{0}_N, (\psi_{l,\text{ICI}}^2 + \psi_{l,\text{ISI}}^2)\mathbf{I}_N)$. Consequently, we will use the values of ISI ($\psi_{l,\text{ISI}}^2$) and ICI powers ($\psi_{l,\text{ICI}}^2$) recorded in Table III depending on the propagation scenario.

Combining the decisions from all the K SUs independently on each sub-carrier, we can arrive at the total probabilities $P_{D_0}^l$ and $P_{F_0}^l$ for the network for our chosen fusion algorithms. To compare the performance of different decision fusion rules both in terms of instantaneous sub-carrier (IS), system false alarm and detection probabilities can be defined as,

$$\begin{aligned} P_{F_0}^l(\gamma^l, \mathbf{G}^l) &\triangleq \Pr\{\mathbf{\Gamma}^l > \gamma^l | \mathbf{G}^l, \mathcal{H}_0^l\} \\ P_{D_0}^l(\gamma^l, \mathbf{G}^l) &\triangleq \Pr\{\mathbf{\Gamma}^l > \gamma^l | \mathbf{G}^l, \mathcal{H}_1^l\} \end{aligned} \tag{14}$$

where γ^l denote the threshold with which the log-likelihood ratio (LLR) is compared to, and $\mathbf{\Gamma}^l$ is the generic statistic employed at the DFC over the lth sub-carrier.

B. Fusion Rules

For comparison of fusion performance of the wideband spectrum sensing network, we consider four different decision fusion rules, Log-likelihood Ratio (LLR) rule, Widely Linear (WL) rules, Maximal Ratio Combining (MRC) and modified MRC (mMRC) rules, proposed in [9], for single frequency carrier system. This set of rules aims at concluding on whether the PU is active or silent directly from the received signal without processing the transmit signal.

1) Log-Likelihood Ratio (LLR) Rule: If the DFC is equipped with large number of receive antennas i.e. $N \gg K$, the LLR test statistics is given by,

$$\mathbf{\Gamma}_{\text{LLR}}^l = \ln\left[\frac{\sum_{\mathbf{x}^l} \exp\left(-\frac{||\mathbf{y}^l - \sqrt{\rho^l}\mathbf{G}^l\mathbf{x}^l||^2}{\sigma_{e,l}^2}\right) P\left(\mathbf{x}^l|\mathcal{H}_1^l\right)}{\sum_{\mathbf{x}^l} \exp\left(-\frac{||\mathbf{y}^l - \sqrt{\rho^l}\mathbf{G}^l\mathbf{x}^l||^2}{\sigma_{e,l}^2}\right) P\left(\mathbf{x}^l|\mathcal{H}_0^l\right)}\right] \tag{15}$$

where $\mathbf{\Gamma}_{\text{LLR}}^l$ is the LLR for the LLR rule, $\sigma_{e,l}^2 \triangleq \sigma_{w,l}^2 + \psi_l^2$, with $\sigma_{w,l}^2$ and ψ_l^2 as the power densities of the noise and interference processes respectively.

2) Widely Linear (WL) Rules: If WL statistics is adopted, $\mathbf{\Gamma}_{i,l}^{\text{WL}} \triangleq (\underline{\mathbf{a}}_{\text{WL},i}^l)^\dagger\underline{\mathbf{y}}^l$ and $\underline{\mathbf{a}}_{\text{WL},i}^l$ is chosen such that the deflection measure is maximized following, $\underline{\mathbf{a}}_{\text{WL},i}^l \triangleq \max_{\underline{\mathbf{a}}^l:||\underline{\mathbf{a}}^l||^2}\mathcal{D}_i(\underline{\mathbf{a}}^l)$, where $\mathcal{D}_i(\underline{\mathbf{a}}^l) \triangleq (\mathbb{E}\{\mathbf{\Gamma}_l^{\text{WL}}|\mathcal{H}_1^l\} - \mathbb{E}\{\mathbf{\Gamma}_l^{\text{WL}}|\mathcal{H}_0^l\})^2/\mathbb{V}\{\mathbf{\Gamma}_l^{\text{WL}}|\mathcal{H}_i^l\}$, $\mathcal{D}_0(\underline{\mathbf{a}}^l)$ and $\mathcal{D}_1(\underline{\mathbf{a}}^l)$ correspond to the normal and modified deflections respectively [4]. If WL statistics is adopted with deflection measures $\mathcal{D}_0(\underline{\mathbf{a}}^l)$ and $\mathcal{D}_1(\underline{\mathbf{a}}^l)$, the corresponding fusion rules will be referred as 'WL,0' and 'WL,1' rules respectively. The expressions for $\underline{\mathbf{a}}_{\text{WL},i}^l$ can be given by,

$$\underline{\mathbf{a}}_{\text{WL},i}^l = \mathbf{\Sigma}_{\underline{\mathbf{y}}^l|\mathbf{G}^l,\mathcal{H}_i^l}^{-1}\underline{\mathbf{G}}^l\boldsymbol{\mu}_i^l \Big/ \left(\left|\left|\mathbf{\Sigma}_{\underline{\mathbf{y}}^l|\mathbf{G}^l,\mathcal{H}_i^l}^{-1}\underline{\mathbf{G}}^l\boldsymbol{\mu}_i^l\right|\right|\right) \tag{16}$$

following the proposition made in [9], where $\mathbf{\Sigma}_{\underline{\mathbf{y}}^l|\mathbf{G}^l,\mathcal{H}_i^l} = \left(\rho^l\underline{\mathbf{G}}^l\mathbf{\Sigma}_{\mathbf{x}^l|\mathcal{H}_i^l}(\underline{\mathbf{G}}^l)^\dagger + \sigma_{e,l}^2\mathbf{I}_{2N}\right)$ and $\boldsymbol{\mu}_i^l \triangleq 2\left[\left(P_{D,1}^l - P_{F,1}^l\right)\ldots\left(P_{D,K}^l - P_{F,K}^l\right)\right]^t$. In order to derive the exact IS system probabilities for this fusion rule, we can define $\mathbf{\Gamma}_{i,\text{WL}}^{l,\text{WB}} \triangleq \frac{\mathbf{\Gamma}_i^{l,\text{WL}}}{\sigma_{e,l}}$ and $\mathbf{\Gamma}_{i,\text{WL}}^{l,\text{WB}}|\mathbf{G}^l, \mathcal{H}_j^l$ is distributed as $\mathbf{\Gamma}_{i,\text{WL}}^{l,\text{WB}}|\mathbf{G}^l, \mathcal{H}_j^l \sim \sum_{\mathbf{x}^l\in\chi^K} P\left(\mathbf{x}^l|\mathcal{H}_j^l\right)\mathcal{N}\left(\mathbb{E}\{\mathbf{\Gamma}_{i,\text{WL}}^{l,\text{WB}}|\mathbf{G}^l, \mathbf{x}^l\}, 1\right)$ where, for a large system,

$$\lim_{N\to\infty}\left(\mathbb{E}\{\mathbf{\Gamma}_{i,\text{WL}}^{l,\text{WB}}|\mathbf{G}^l, \mathbf{x}^l\}\right) = \frac{N\sqrt{2\rho^l}(\boldsymbol{\mu}_i^l)^t\mathbf{x}^l\mathbf{V}_i^l\mathbf{D}_g^l}{\sigma_{e,l}\sqrt{(\boldsymbol{\mu}_i^l)^t\mathbf{V}_i^l\mathbf{D}_g^l(\mathbf{V}_i^l)^t\boldsymbol{\mu}_i^l}} \tag{17}$$

where

$$\mathbf{V}_i^l \triangleq \mathbf{I}_K - \left(\frac{1+\sigma_{w,l}^2+\sum_{k=1}^K\overline{\tau}_{l,k}^2+\sum_{k=1}^K\sum_{p=1}^L\left|\overline{\beta}_k^p(d_{pl})\right|^2}{2\mathbf{D}_g^l\rho^l N\sqrt{N}\mathbf{\Sigma}_{\mathbf{x}^l|\mathcal{H}_i^l}^{-1}}\right)^{-1} \tag{18}$$

for $l \neq p$ and $\mathbf{D}_g^l = \mathbf{D} * [\text{diag}(\mathcal{B}_k^l)]$.

3) Maximal Ratio Combining (MRC) Rules: The LLR in (15) can be simplified under the MRC fusion rule, i.e. $P(\mathbf{x}^l = \mathbf{1}_K|\mathcal{H}_1^l) = P(\mathbf{x}^l = -\mathbf{1}_K|\mathcal{H}_0^l) = 1$. In this case, $\mathbf{x}^l \in \{\mathbf{1}_K, -\mathbf{1}_K\}$ and (15) reduces to,

$$\ln\left[\frac{\exp\left(-\frac{||\mathbf{y}^l - \sqrt{\rho^l}\mathbf{G}^l\mathbf{1}_K||^2}{\sigma_{e,l}^2}\right)}{\exp\left(-\frac{||\mathbf{y}^l + \sqrt{\rho^l}\mathbf{G}^l\mathbf{1}_K||^2}{\sigma_{e,l}^2}\right)}\right] \propto \mathbb{R}\left\{\left(\mathbf{a}_{\text{MRC}}^l\right)^\dagger\mathbf{y}^l\right\} \triangleq \mathbf{\Gamma}_{\text{MRC}}^l \tag{19}$$

where, $\mathbf{a}_{\text{MRC}}^l \triangleq \mathbf{G}^l\mathbf{1}_K$. In this case, we can define, $\mathbf{\Gamma}_{\text{MRC}}^{l,\text{WB}} \triangleq \frac{\sqrt{2}\mathbf{\Gamma}_{\text{MRC}}^l}{\sigma_{e,l}\,||\mathbf{a}_{\text{MRC}}^l||}$ and evaluate the performance in terms of $\mathbf{\Gamma}_{\text{MRC}}^{l,\text{WB}}$. In that case,

$$\mathbb{E}\{\mathbf{\Gamma}_{\text{MRC}}^{l,\text{WB}}|\mathbf{G}^l, \mathbf{x}^l\} = \frac{\sqrt{2\rho^l}\,\mathbb{R}\{(\mathbf{1}_K)^t(\mathbf{G}^l)^\dagger\mathbf{G}^l\mathbf{x}^l\}}{\sigma_{e,l}\sqrt{(\mathbf{1}_K)^t(\mathbf{G}^l)^\dagger\mathbf{G}^l\mathbf{1}_K}} \tag{20}$$

where for a large system, i.e. as $N \to \infty$,

$$\lim_{N\to\infty}\left(\mathbb{E}\{\mathbf{\Gamma}_{\text{MRC}}^{l,\text{WB}}|\mathbf{G}^l, \mathbf{x}^l\}\right) = \frac{\sqrt{2\,N\rho^l}\,\mathbb{R}\{(\mathbf{1}_K)^t\mathbf{D}_g^l\mathbf{x}^l\}}{\sigma_{e,l}\sqrt{(\mathbf{1}_K)^t\mathbf{D}_g^l\mathbf{1}_K}} \tag{21}$$

Additionally, in order to exploit the linear SINR increase with N, we can resort to an alternative form of MRC,

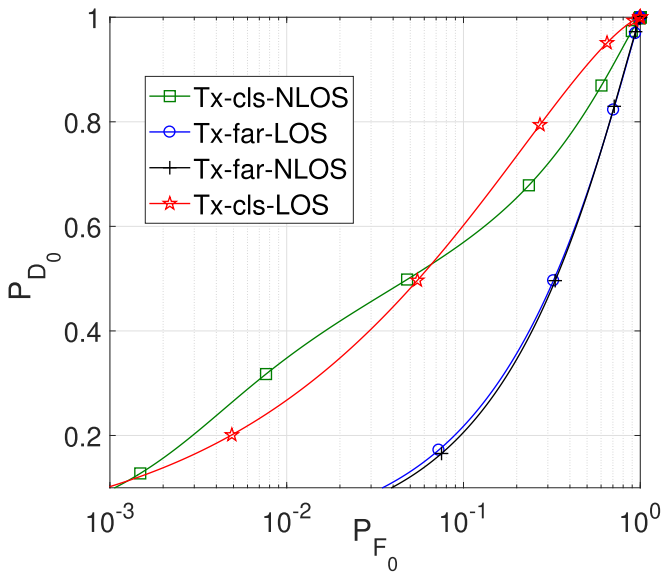

Fig. 10. Comparative ROC for the LLR fusion rule for different measured large scale parameters (varying ν, μ_λ and σ_λ) with $K = 4$, $N = 64$ and Rayleigh distributed fading vector.

denoted as modified MRC (mMRC) given by, $\mathbf{\Gamma}^l_{\text{mMRC}} \triangleq \mathbb{R}\{(\mathbf{a}^l_{\text{mMRC}})^\dagger \mathbf{y}^l\}$ where, $\mathbf{a}^l_{\text{mMRC}} \triangleq \mathbf{G}^l(\mathbf{D}^l_g)^{-1}\mathbf{1}_K$. We define, $\mathbf{\Gamma}^{l,\text{WB}}_{\text{mMRC}} \triangleq \frac{\sqrt{2}\mathbf{\Gamma}^l_{\text{mMRC}}}{\sigma_{e,l}\ ||\mathbf{a}^l_{\text{mMRC}}||}$ and evaluate the performance in terms of $\mathbf{\Gamma}^{l,\text{WB}}_{\text{mMRC}}$ as,

$$\lim_{N\to\infty}\left(\mathbb{E}\{\mathbf{\Gamma}^{l,\text{WB}}_{\text{mMRC}}|\mathbf{G}^l,\mathbf{x}^l\}\right) = \frac{\sqrt{2\ N\rho^l}\ \mathbb{R}\{(\mathbf{1}_K)^t\mathbf{x}^l\}}{\sigma_{e,l}\sqrt{(\mathbf{1}_K)^t(\mathbf{D}^l_g)^{-1}\mathbf{1}_K}} \quad (22)$$

for a large system.

C. Time-Reversal (TR) Based Fusion Rules

Achievable SINR saturates at a certain deterministic level in absence of CP if conventional DF rules like MRC, Zero Forcing (ZF), etc. are used at the DFC equipped with a massive antenna array. This happens due to the correlation between the combiner taps and the additional interference components which do not average out with the increase in the number of receive and/or transmit antennas. In this section, we propose application of time-reversal (TR) methods to alleviate this saturation problem. In order to exploit advantages of TR methods when applied to large array regime, we propose application of TR-WL and TR-MRC fusion rules in collaborative WSS.

1) TR-WL Rule: The first approach consists of adopting the TR variant of the WL statistics such that, $\mathbf{\Gamma}^{\text{TR-WL}}_{i,l} \triangleq (\underline{\mathbf{a}}^l_{\text{TR-WL},i})^\dagger \underline{\mathbf{y}}^l$ where $\underline{\mathbf{a}}^l_{\text{TR-WL},i}$ can be explicitly expressed as,

$$\underline{\mathbf{a}}^l_{\text{TR-WL},i} = \mathbf{\Sigma}^{-1}_{\underline{\mathbf{y}}^l|\breve{\mathbf{G}}^l,\mathcal{H}^l_i}\breve{\underline{\mathbf{G}}}^l\boldsymbol{\mu}^l_i \Big/ \left(\left|\left|\mathbf{\Sigma}^{-1}_{\underline{\mathbf{y}}^l|\breve{\mathbf{G}}^l,\mathcal{H}^l_i}\breve{\underline{\mathbf{G}}}^l\boldsymbol{\mu}^l_i\right|\right|\right) \quad (23)$$

following the formulation and proposition made in Subsection IV-A, where $\mathbf{\Sigma}_{\underline{\mathbf{y}}^l|\breve{\mathbf{G}}^l,\mathcal{H}^l_i} = \left(\rho^l\breve{\underline{\mathbf{G}}}^l\mathbf{\Sigma}_{\mathbf{x}^l|\mathcal{H}^l_i}(\breve{\underline{\mathbf{G}}}^l)^\dagger + \sigma^2_{e,l}\mathbf{I}_{2N}\right)$. Using the definition, $\mathbf{\Gamma}^{l,\text{WB}}_{i,\text{TR-WL}} \triangleq \frac{\mathbf{\Gamma}^{l,\text{TR-WL}}_i}{\sigma_{e,l}}$ and the test statistics $\mathbf{\Gamma}^{l,\text{TR-WL}}_i$ being distributed as $\mathbf{\Gamma}^{l,\text{TR-WL}}_i|\mathbf{G}^l,\mathbf{x}^l \sim \mathcal{N}(\mathbb{E}\{\mathbf{\Gamma}^{l,\text{TR-WL}}_i|\mathbf{G}^l,\mathbf{x}^l\},\mathbb{V}\{\mathbf{\Gamma}^{l,\text{TR-WL}}_i|\mathbf{G}^l,\mathbf{x}^l\})$, $\mathbf{\Gamma}^{l,\text{WB}}_{i,\text{TR-WL}}|\mathbf{G}^l,\mathcal{H}^l_j$ will be distributed as $\mathbf{\Gamma}^{l,\text{WB}}_{i,\text{TR-WL}}|\mathbf{G}^l,\mathcal{H}^l_j \sim \sum_{\mathbf{x}^l\in\chi^K} P(\mathbf{x}^l|\mathcal{H}^l_j)\mathcal{N}(\mathbb{E}\{\mathbf{\Gamma}^{l,\text{WB}}_{i,\text{TR-WL}}|\mathbf{G}^l,\mathbf{x}^l\},1)$. Here,

$$\mathbb{E}\{\mathbf{\Gamma}^{l,\text{WB}}_{i,\text{TR-WL}}|\mathbf{G}^l,\mathbf{x}^l\} = \frac{\sqrt{2\rho^l}(\boldsymbol{\mu}^l_i)^t(\underline{\mathbf{G}}^l)^\dagger\mathbf{\Sigma}^{-1}_{\underline{\mathbf{y}}^l|\breve{\mathbf{G}}^l,\mathcal{H}^l_i}\breve{\underline{\mathbf{G}}}^l\mathbf{x}^l}{\sigma_{e,l}||\mathbf{\Sigma}^{-1}_{\underline{\mathbf{y}}^l|\breve{\mathbf{G}}^l,\mathcal{H}^l_i}\breve{\underline{\mathbf{G}}}^l\mathbf{x}^l||} \quad (24)$$

As $N\to\infty$, we have,

$$\lim_{N\to\infty}\left(\mathbb{E}\{\mathbf{\Gamma}^{l,\text{WB}}_{i,\text{WL}}|\mathbf{G}^l,\mathbf{x}^l\}\right) = \frac{N\sqrt{2\rho^l}(\boldsymbol{\mu}^l_i)^t\mathbf{x}^l\breve{\mathbf{V}}^l_i\mathbf{F}^l}{\sigma_{e,l}\sqrt{(\boldsymbol{\mu}^l_i)^t\breve{\mathbf{V}}^l_i\breve{\mathbf{A}}^l(\breve{\mathbf{V}}^l_i)^t\boldsymbol{\mu}^l_i}} \quad (25)$$

where

$$\breve{\mathbf{V}}^l_i \triangleq \mathbf{I}_K - \left(\frac{1+\sigma^2_{w,l}+\sum_{k=1}^K\overline{\tau}^2_{l,k}+\sum_{k=1}^K\sum_{p=1}^L\left|\overline{\beta}^p_k(d_{pl})\right|^2}{2\breve{\mathbf{A}}^l\rho^lN\sqrt{N}\mathbf{\Sigma}^{-1}_{\mathbf{x}^l|\mathcal{H}^l_i}}\right)^{-1}$$

for $l\neq p$.

2) TR-MRC Rules: The TR-MRC rule can be defined as, $\mathbf{a}^l_{\text{TR-MRC}} \triangleq \breve{\mathbf{G}}^l\mathbf{1}_K$, and the test statistics as, $\mathbf{\Gamma}^{l,\text{WB}}_{\text{TR-MRC}} \triangleq \frac{\sqrt{2}\mathbf{\Gamma}^l_{\text{TR-MRC}}}{\sigma_{e,l}\ ||\mathbf{a}^l_{\text{TR-MRC}}||}$ and,

$$\mathbb{E}\{\mathbf{\Gamma}^{l,\text{WB}}_{i,\text{TR-MRC}}|\mathbf{G}^l,\mathbf{x}^l\} = \frac{\sqrt{2\ N\rho^l}\ \mathbb{R}\{(\mathbf{1}_K)^t\mathbf{F}^l\mathbf{x}^l\}}{\sigma_{e,l}\sqrt{(\mathbf{1}_K)^t\breve{\mathbf{A}}^l\mathbf{1}_K}} \quad (26)$$

for $N\to\infty$. In order to exploit the linear SINR increase with N, we devise an alternative form of mMRC, denoted as time-reversed modified MRC (TR-mMRC) given by, $\mathbf{\Gamma}^l_{\text{TR-mMRC}} \triangleq \mathbb{R}\{(\mathbf{a}^l_{\text{TR-mMRC}})^\dagger\mathbf{y}^l\}$ where, $\mathbf{a}^l_{\text{TR-mMRC}} \triangleq \breve{\mathbf{G}}^l(\breve{\mathbf{A}}^l)^{-1}\mathbf{1}_K$. Thus we can define, $\mathbf{\Gamma}^{l,\text{WB}}_{\text{TR-mMRC}} \triangleq \frac{\sqrt{2}\mathbf{\Gamma}^l_{\text{TR-mMRC}}}{\sigma_{e,l}\ ||\mathbf{a}^l_{\text{TR-mMRC}}||}$ and, in case of $N\in\infty$, evaluate the performance in terms of $\mathbf{\Gamma}^{l,\text{WB}}_{\text{TR-mMRC}}$ as,

$$\mathbb{E}\{\mathbf{\Gamma}^{l,\text{WB}}_{i,\text{TR-mMRC}}|\mathbf{G}^l,\mathbf{x}^l\} = \frac{\sqrt{2\ N\rho^l}\ \mathbb{R}\{(\mathbf{1}_K)^t(\breve{\mathbf{G}}^l)^\dagger((\breve{\mathbf{A}}^l)^{-1})^\dagger\mathbf{G}^l\mathbf{x}^l\}}{\sigma_{e,l}\sqrt{(\mathbf{1}_K)^t((\breve{\mathbf{A}}^l)^{-1})^\dagger\mathbf{1}_K}} \quad (27)$$

D. Performance Analysis

Assuming $\mathbb{E}\{\mathbf{x}^l|\mathcal{H}^l_0\} \triangleq (2\ P^l_F - 1)\mathbf{1}_K$ and $\mathbb{E}\{(\mathbf{x}^l - \mathbb{E}\{\mathbf{x}^l|\mathcal{H}^l_0\})(\mathbf{x}^l - \mathbb{E}\{\mathbf{x}^l|\mathcal{H}^l_0\})^t|\mathcal{H}^l_0\} \triangleq [1-(2\ P^l_F-1)^2]\mathbf{I}_K$, we can compute $P^l_{F_0}$ for both WL and MRC set of rules as below. It is to be noted here that, we can also compute $P^l_{D_0}$ by assuming, $\mathbb{E}\{\mathbf{x}^l|\mathcal{H}^l_1\} \triangleq (2\ P^l_D - 1)\mathbf{1}_K$ and $\mathbb{E}\{(\mathbf{x}^l - \mathbb{E}\{\mathbf{x}^l|\mathcal{H}^l_1\})(\mathbf{x}^l - \mathbb{E}\{\mathbf{x}^l|\mathcal{H}^l_1\})^t|\mathcal{H}^l_1\} \triangleq [1-(2\ P^l_D-1)^2]\mathbf{I}_K$.

We first start with the argument that since $P(\mathbf{y}^l|\mathbf{G}^l,\mathcal{H}^l_i)$ is assumed to follow Gaussian mixture distribution, $\mathbf{\Gamma}^{l,\text{WB}}_{i,\text{rule}}|\mathbf{G}^l,\mathcal{H}^l_i$ is also distributed according to Gaussian mixture model that is,

$$\mathbf{\Gamma}^{l,\text{WB}}_{i,\text{rule}}|\mathbf{G}^l,\mathcal{H}^l_i \sim \sum_{\mathbf{x}^l\in\chi^K}P(x^l|\mathcal{H}^l_i) \times\mathcal{N}\left(\mathbb{E}\{\mathbf{\Gamma}^{l,\text{WB}}_{i,\text{rule}}|\mathbf{G}^l,\mathbf{x}^l\},\mathbb{V}\{\mathbf{\Gamma}^{l,\text{WB}}_{i,\text{rule}}|\mathbf{G}^l,\mathbf{x}^l\}\right) \quad (28)$$

Using Gaussian moment matching [37], we can approximate the pdf in (28) as,

$$\mathbf{\Gamma}^{l,\mathrm{WB}}_{i,\mathrm{rule}}|\mathbf{G}^l,\mathcal{H}^l_i \overset{\text{approx}}{\sim} \mathcal{N}\big(\mathbb{E}\{\mathbf{\Gamma}^{l,\mathrm{WB}}_{i,\mathrm{rule}}|\mathbf{G}^l,\mathcal{H}^l_i\},\mathbb{V}\{\mathbf{\Gamma}^{l,\mathrm{WB}}_{i,\mathrm{rule}}|\mathbf{G}^l,\mathcal{H}^l_i\}\big). \tag{29}$$

Since at low-SINR, the components of the Gaussian mixture gets concentrated within a certain region, we need to evaluate the mean and variance of $\mathbf{\Gamma}^{l,\mathrm{WB}}_{i,\mathrm{rule}}|\mathbf{G}^l,\mathcal{H}^l_i$ separately for the WL and MRC rules. For this purpose, let us define, $\tilde{\mathbf{G}}^l \triangleq \big[\mathbf{G}^{l\,t}\ \ \mathbf{G}^{l\,\dagger}\big]^t$ and $\tilde{\mathbf{a}}^l_{\mathrm{m}} \triangleq \frac{1}{2}\big[\mathbf{a}^{l\ t}_{\mathrm{m}}\ \ \mathbf{a}^{l\ \dagger}_{\mathrm{m}}\big]^t$, where $\mathbf{a}^l_{\mathrm{m}}$ is either $\mathbf{a}^l_{\mathrm{MRC}}$, $\mathbf{a}^l_{\mathrm{mMRC}}$ or $\mathbf{a}^l_{\text{TR-mMRC}}$ depending on the fusion rules chosen from the set of MRC and TR-MRC rules.

Here we evaluate the mean and variance of $\mathbf{\Gamma}^{l,\mathrm{WB}}_{i,\mathrm{WL}}|\mathbf{G}^l,\mathcal{H}^l_i$ as,

$$\mathbb{E}\big\{\mathbf{\Gamma}^{l,\mathrm{WB}}_{i,\mathrm{WL}}|\mathbf{G}^l,\mathbf{x}^l\big\} = \frac{\sqrt{\rho^l}(\mu^l_i)^t(\mathbf{G}^l)^\dagger\mathbf{\Sigma}^{-1}_{\mathbf{y}^l|\mathbf{G}^l,\mathcal{H}^l_i}\mathbf{G}^l\ \mathbb{E}\{\mathbf{x}^l|\mathcal{H}^l_i\}}{||\mathbf{\Sigma}^{-1}_{\mathbf{y}^l|\mathbf{G}^l,\mathcal{H}^l_i}\mathbf{G}^l\mathbf{x}^l||} \tag{30}$$

and

$$\begin{aligned}\mathbb{V}\big\{\mathbf{\Gamma}^{l,\mathrm{WB}}_{i,\mathrm{WL}}|\mathbf{G}^l,\mathbf{x}^l\big\} &= \sum_{\mathbf{x}^l\in\chi^K}\tilde{\mathbf{G}}^l\ \mathbb{E}\{(\mathbf{x}^l-\mathbb{E}\{\mathbf{x}^l|\mathcal{H}^l_i\})\\ &\quad\times(\mathbf{x}^l-\mathbb{E}\{\mathbf{x}^l|\mathcal{H}^l_i\})^T|\mathcal{H}^l_i\}(\tilde{\mathbf{G}}^l)^\dagger+2\sigma^2_{e,l}\end{aligned} \tag{31}$$

Under simplifying assumptions of $\mathbb{E}\{\mathbf{x}^l|\mathcal{H}^l_0\} = (2\ P^l_F-1)\mathbf{1}_K$ (31) becomes,

$$\begin{aligned}\mathbb{V}\big\{\mathbf{\Gamma}^{l,\mathrm{WB}}_{i,\mathrm{WL}}|\mathbf{G}^l,\mathbf{x}^l\big\} &= [1-(2\ P^l_F-1)^2]\tilde{\mathbf{G}}^l(\tilde{\mathbf{G}}^l)^\dagger+2\sigma^2_{e,l}\\ &\approx \lim_{K\to\infty}2(1-\delta^{l\,2})K+2\sigma^2_{e,l}\end{aligned} \tag{32}$$

where $\delta^l = (2\ P^l_F-1)$. Using (30) and (32) and exploiting (29), we obtain the low-SINR approximation for $P^l_{F_0}$ as,

$$P^{l,\mathrm{WL}}_{F_0} \approx \lim_{N\to\infty} Q\left(\frac{\gamma^l-\frac{N\delta^l\sqrt{2\rho^l}(\mu^l_i)^t\mathbf{x}^l\mathbf{V}^l_i\mathbf{D}^l_g}{\sigma_{e,l}\sqrt{(\mu^l_i)^t\mathbf{V}^l_i\mathbf{D}^l_g(\mathbf{V}^l_i)^t\mu^l_i}}}{\sqrt{2(1-\delta^{l\,2})K+2\sigma^2_{e,l}}}\right) \tag{33}$$

Next, we find the mean and variance of $\mathbf{\Gamma}^{l,\mathrm{WB}}_{i,\mathrm{m}}|\mathbf{G}^l,\mathcal{H}^l_i$ as,

$$\mathbb{E}\big\{\mathbf{\Gamma}^{l,\mathrm{WB}}_{i,\mathrm{m}}|\mathbf{G}^l,\mathbf{x}^l\big\} = \sqrt{\rho^l}\mathbb{R}\big\{(\mathbf{a}^l_{\mathrm{m}})^\dagger\mathbf{G}^l\ \mathbb{E}\{\mathbf{x}^l|\mathcal{H}^l_i\}\big\} \tag{34}$$

and

$$\begin{aligned}\mathbb{V}\big\{\mathbf{\Gamma}^{l,\mathrm{WB}}_{i,\mathrm{m}}|\mathbf{G}^l,\mathbf{x}^l\big\} &= \sum_{\mathbf{x}^l\in\chi^K}(\tilde{\mathbf{a}}^l_{\mathrm{m}})^\dagger\tilde{\mathbf{G}}^l\ \mathbb{E}\{(\mathbf{x}^l-\mathbb{E}\{\mathbf{x}^l|\mathcal{H}^l_i\})\\ &\quad\times(\mathbf{x}^l-\mathbb{E}\{\mathbf{x}^l|\mathcal{H}^l_i\})^T|\mathcal{H}^l_i\}(\tilde{\mathbf{G}}^l)^\dagger\tilde{\mathbf{a}}^l_{\mathrm{m}}+\frac{\sigma^2_{e,l}}{2}||\mathbf{a}^l_{\mathrm{m}}||^2\end{aligned} \tag{35}$$

where m represents MRC, mMRC, TR-MRC or TR-mMRC rules. Under simplifying assumptions of $\mathbb{E}\{\mathbf{x}^l|\mathcal{H}^l_0\} = (2\ P^l_F-1)\mathbf{1}_K$ (35) becomes,

$$\mathbb{V}\big\{\mathbf{\Gamma}^{l,\mathrm{WB}}_{i,\mathrm{m}}|\mathbf{G}^l,\mathbf{x}^l\big\} \approx \lim_{K\to\infty}\sqrt{1/2((1-\delta^{l\,2})K+\sigma^2_{e,l})}\ ||\mathbf{a}^l_{\mathrm{m}}|| \tag{36}$$

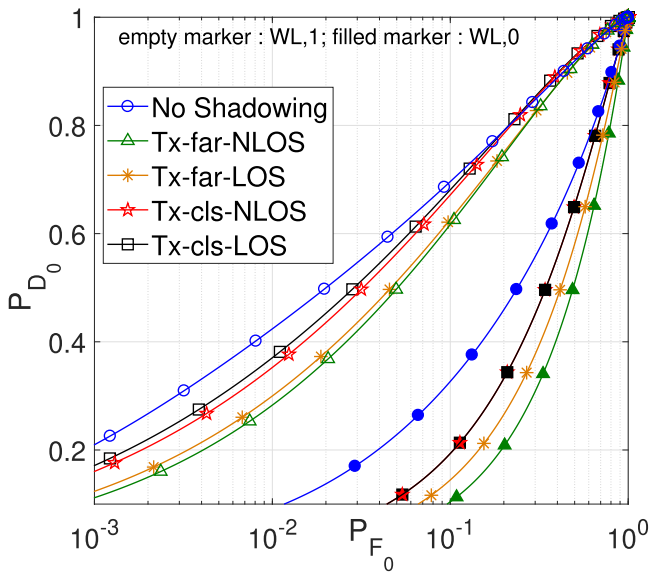

Fig. 11. Comparative ROC for the WL fusion rule for different measured large scale parameters (varying ν, μ_λ and σ_λ) with $K=4$, $N=64$ and Rayleigh distributed fading vector.

where $\delta^l = (2\ P^l_F-1)$. Using (34) and (36) and exploiting (29), we obtain the low-SINR approximation for $P^l_{F_0}$ as,

$$P^{l,m}_{F_0} \approx \lim_{N\to\infty} Q\left(\frac{\gamma^l-\sqrt{N\rho^l}\delta^l||\mathbf{a}^l_{\mathrm{m}}||^2}{\sqrt{1/2((1-\delta^{l\,2})K+\sigma^2_{e,l})}\ ||\mathbf{a}^l_{\mathrm{m}}||}\right). \tag{37}$$

E. Performance Comparison

The fusion performance of a large scale MIMO-based WSN is investigated in this subsection over realistically distributed MIMO mobile radio channels. We will use Rician distribution to generate the channel fading vectors according to (13) for all scenarios with different ranges of K-factors for emulating each scenario.

1) Receiver Operating Characteristics (ROC): This section presents the Receiver Operating Characteristics (ROC) (i.e., P_{D_0} v/s P_{F_0}) plots for the four fusion rules (one optimal and three sub-optimal) propounded in Subsection IV-B with $K=4$ and $N=64$ with an average channel SINR of 25 dB. The chosen SINR is the direct consequence of the average values of the measured noise and interference power, transmit signal power and the average attenuation calculated.

For the curves in Fig. 10, Fig. 11 and Fig. 12, we consider the fading vectors $h^l_{n,k} \sim \mathcal{N}_{\mathbb{C}}(0,1)$ to be Rayleigh distributed. For the 'No shadowing' case in Fig. 11, we resort to $(\eta,\mu_\lambda,\sigma_\lambda) = (1, 0\text{ dB}, 0\text{ dB})$. For all other results, in Fig. 10, Fig. 11 and Fig. 12, we use data from Table-I. According to Fig. 10, presence of LOS components does not have any positive impact on the LLR rule, while closeness of the SUs do. The reason can be the fact that here we concentrate on the large scale channel parameters while small scale parameters are kept constant. In contrast, suboptimal rules like WL, MRC and mMRC do derive advantage of the presence of the LOS components and smaller inter-SU distances (Fig. 11 and Fig. 12). The performance improvement depends on the ability of the fusion rules to make more use of the system knowledge (probability of correct detection, miss-detection

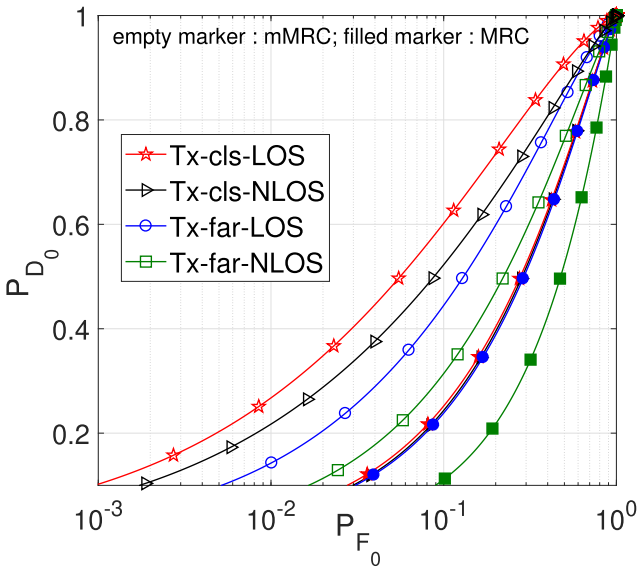

Fig. 12. Comparative ROC for the MRC and mMRC fusion rules for different measured large scale parameters (varying ν, μ_λ and σ_λ) with $K = 4$, $N = 64$ and Rayleigh distributed fading vector.

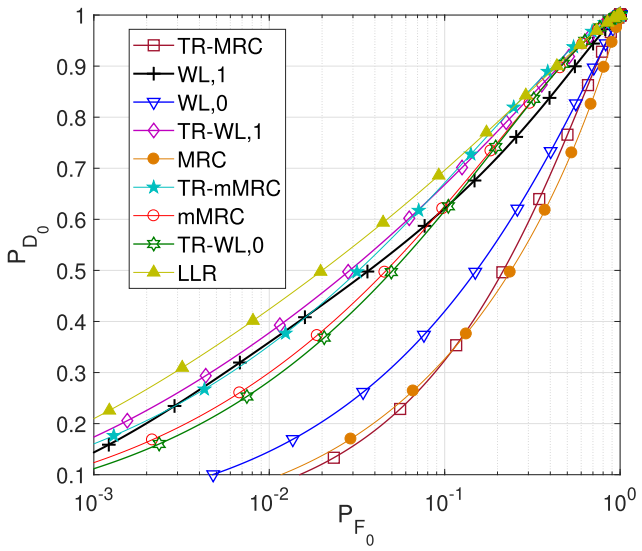

Fig. 13. Comparative ROC for all the fusion rules along with their TR versions for the Tx-cls-LOS scenario with $K = 4$, $N = 64$ accounting for both large and small scale channel effects.

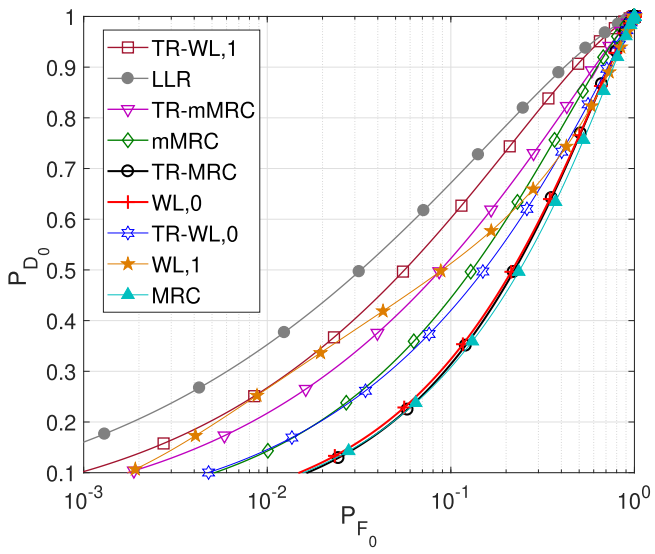

Fig. 14. Comparative ROC for all the fusion rules along with their TR versions for the Tx-cls-NLOS scenario with $K = 4$, $N = 64$ accounting for both large and small scale channel effects.

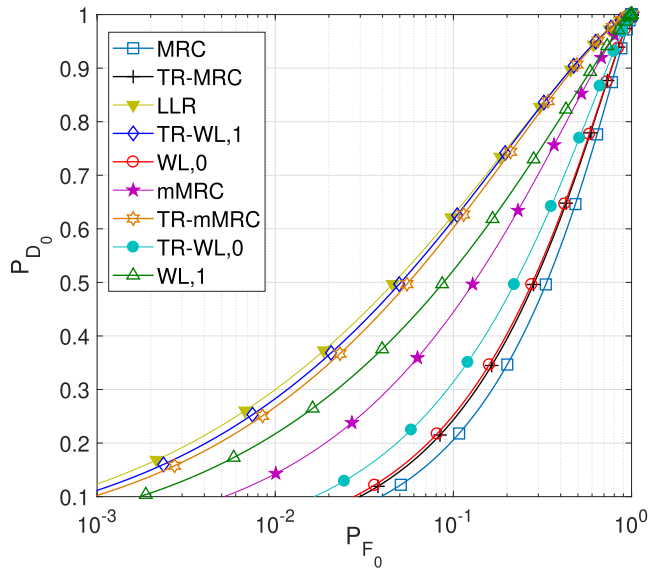

Fig. 15. Comparative ROC for all the fusion rules along with their TR versions for the Tx-far-LOS scenario with $K = 4$, $N = 64$ accounting for both large and small scale channel effects.

or false-alarm) and environment (shadowing, fading, noise, interference) statistics.

In order to ameliorate performance degradation resulting from the availability of reduced system knowledge and introduction of interference due to channel impairments, we have introduced TR-based fusion rules in Section IV-C. In Fig. 13, we compare fusion performance of different formulated fusion rules with their TR-versions over 4×64 MIMO channel with Rician distributed vector and large scale parameters equivalent to Tx-cls-LOS scenario i.e. $(\eta, \mu_\lambda, \sigma_\lambda) = (2.51, -1.43 \text{ dB}, -4.9 \text{ dB})$. The channel parameters κ_k^l, $\psi_{l,\text{ISI}}^2$ and $\psi_{l,\text{ICI}}^2$ are randomly generated in the ranges $[\kappa_{k,\min}^l, \kappa_{k,\max}^l] = [8, 9]$, $[\psi_{l,\text{ISI, min}}^2, \psi_{l,\text{ISI, max}}^2] = [-55 \text{ dB}, -35 \text{ dB}]$ and $[\psi_{l,\text{ICI, min}}^2, \psi_{l,\text{ICI, max}}^2] = [-60 \text{ dB}, -50 \text{ dB}]$ respectively. For Fig. 14, we use $[\kappa_{k,\min}^l, \kappa_{k,\max}^l] = [1.1, 5]$, $[\psi_{l,\text{ISI, min}}^2, \psi_{l,\text{ISI, max}}^2] = [-55 \text{ dB}, -35 \text{ dB}]$ and $[\psi_{l,\text{ICI, min}}^2, \psi_{l,\text{ICI, max}}^2] = [-74 \text{ dB}, -36 \text{ dB}]$ and large scale parameters $(\eta, \mu_\lambda, \sigma_\lambda) = (2.37, 3.01 \text{ dB}, 0.57 \text{ dB})$. equivalent to Tx-cls-NLOS. For Fig. 15, we choose $[\kappa_{k,\min}^l, \kappa_{k,\max}^l] = [3, 11]$, $[\psi_{l,\text{ISI, min}}^2, \psi_{l,\text{ISI, max}}^2] = [-55 \text{ dB}, -35 \text{ dB}]$ and $[\psi_{l,\text{ICI, min}}^2, \psi_{l,\text{ICI, max}}^2] = [-66 \text{ dB}, -44 \text{ dB}]$ and $(\eta, \mu_\lambda, \sigma_\lambda) = (2.93, 3.42 \text{ dB}, 3.54 \text{ dB})$ corresponding to Tx-far-LOS and for Fig. 16, we resort to $[\kappa_{k,\min}^l, \kappa_{k,\max}^l] = [0.75, 4]$, $[\psi_{l,\text{ISI, min}}^2, \psi_{l,\text{ISI, max}}^2] = [-54 \text{ dB}, -36 \text{ dB}]$ and $[\psi_{l,\text{ICI, min}}^2, \psi_{l,\text{ICI, max}}^2] = [-65 \text{ dB}, -45 \text{ dB}]$ and $(\eta, \mu_\lambda, \sigma_\lambda) = (3.12, 5.83 \text{ dB}, 5.05 \text{ dB})$ according to the values obtained for Tx-far-NLOS.

From Fig. 13 - Fig. 16, it can be summarized that WL,1 yields the best results after the LLR rule with MRC

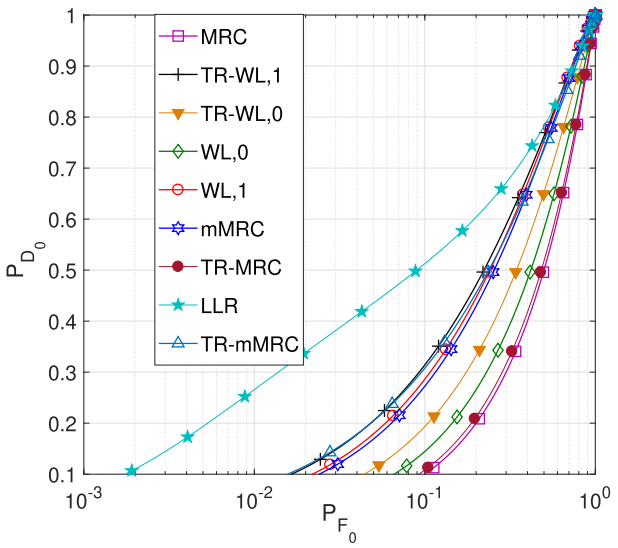

Fig. 16. Comparative ROC for all the fusion rules along with their TR versions for the Tx-far-NLOS scenario with $K = 4$, $N = 64$ accounting for both large and small scale channel effects.

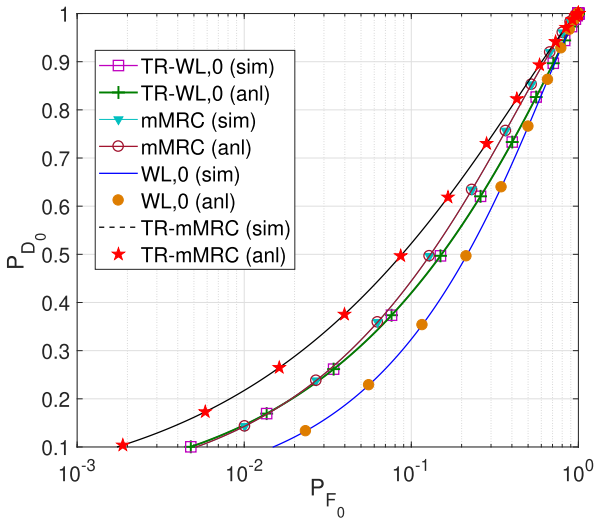

Fig. 17. Comparative analytical ('anl') and simulation ('sim') performance for mMRC, TR-mMRC, WL,0 and TR-WL,0 rules in the Tx-cls-NLOS scenario with $K = 4$, $N = 64$.

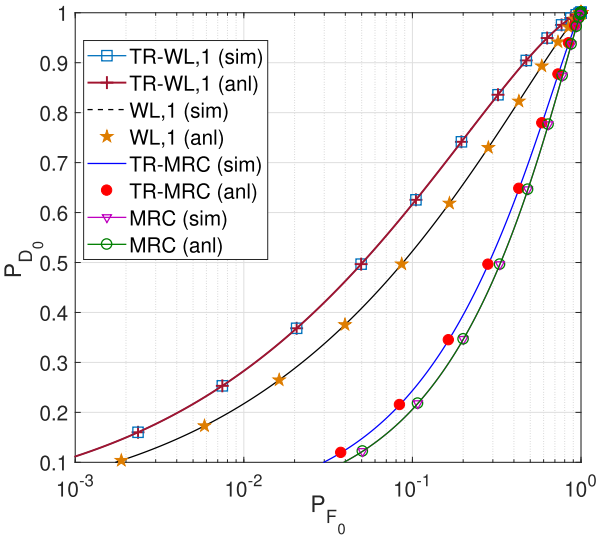

Fig. 18. Comparative analytical ('anl') and simulation ('sim') performance for MRC, TR-MRC, WL,1 and TR-WL,1 rules in the Tx-far-LOS scenario with $K = 4$, $N = 64$.

yielding the worst performance. The mMRC rule always performs better than WL,0 and MRC as mMRC utilizes more system information than MRC, like fading and shadowing statistics, PDP etc. This is in contrary to the observations in [9] where the performance is simulated over a synthetic environment. On the other hand, WL,1 performs better than WL,0 owing to its ability to exploit properties of more statistical events observed; WL,0 employs characterization of $\mathbf{\Sigma}_{\mathbf{x}^l|\mathcal{H}_0^l}$ while WL,1 utilizes knowledge on $\mathbf{\Sigma}_{\mathbf{x}^l|\mathcal{H}_1^l}$. This is in accordance with the observations made in [9]. For large N, both TR-MRC and TR-mMRC outperform MRC and mMRC. It is also apparent that even when the SUs are far from each other, TR variants of WL and MRC become more appealing solutions than ordinary MRC or WL. However, TR-WL,1 offers better performance than TR-mMRC and TR-WL,0 performs better than TR-MRC. If no direct LOS communication path exists between the SUs and the DFC, TR-MRC and TR-mMRC offers negligible performance improvement over their non-TR versions. The advantage offered by TR-mMRC over TR-WL,0 can be attributed to the fact that mMRC exploits SINR increase for large N. The mMRC rule utilizes the channel PDP to compute the test statistics, while WL,0 only uses the characterization of $\mathbf{\Sigma}_{\mathbf{x}^l|\mathcal{H}_0^l}$. When a large range of interfering power values are encountered, TR-mMRC performs better than TR-WL,0, as mMRC takes advantage of more system knowledge like fading statistics and PDP vectors.

Fig. 16 demonstrates that TR-based rules offer very limited improvement in performance over the non-TR ones for the case where the SUs are far apart without any LOS path existing between the SUs and the DFC. The reason can be the fact that TR-based methods take advantage of the degrees of freedom offered by the propagation environment; the larger the number of multipaths, the better is the fight against additional interference experienced. However, the present measurement campaign, as conducted in an indoor-only environment, can only experience a limited number of multipaths arriving at the DFC. Such a small number of multipath components may not be enough to derive additional information regarding the propagation environment.

It is noteworthy that, channel measurements collected in any other environment can be directly incorporated into the system modelling equations and fusion rule formulations, presented in this paper, to obtain performance analysis in that particular environment. With the aim of generalization, we have derived equations to evaluate performance of the formulated fusion rules numerically in Section IV-D. We also establish the validity of our derived expressions by comparing simulated and analytical performance of different fusion rules in Fig. 17 and Fig. 18. The analytical performances match closely, and many cases, almost identical to the simulated performances. The reason can be attributed to the fact that the channel samples for the analytical results are generated using the same Ricean channel model (refer to (13)), as is used for generating the simulation results. This is done to replicate the

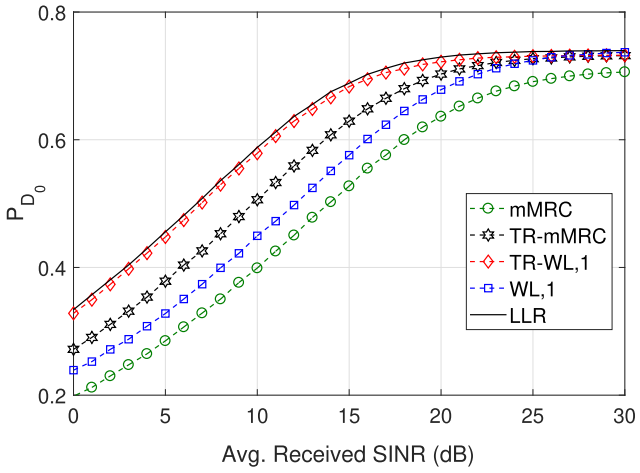

Fig. 19. P_{D_0} v/s SINR for the case when the SUs are separated by partitions (glass or dry-wall) in a LOS scenario.

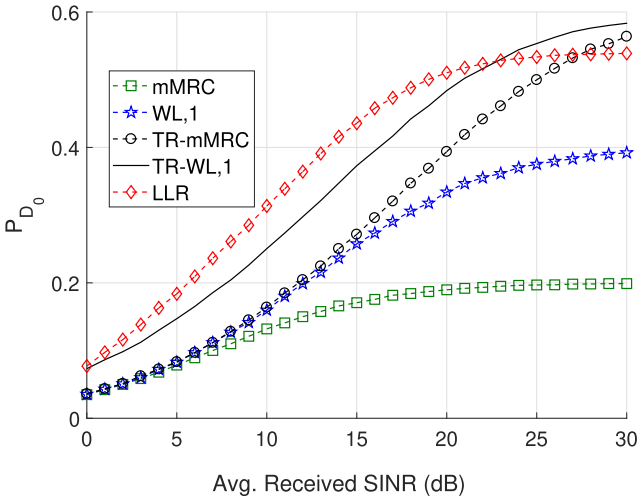

Fig. 20. P_{D_0} v/s SINR for the case when the SUs are separated by partitions (glass or dry-wall) in a NLOS scenario.

practical propagation scenario as precisely as possible using the accumulated measurement data.

2) P_{D_0} v/s SINR (dB): In Fig. 19 and Fig. 20, we plot the P_{D_0} for the fusion rules, that come out to be the winners in different kinds of scenarios (LLR, WL,1, TR-WL,1, mMRC and TR-mMRC), as a function of the received SINR with $P_{F_0} \leq 0.01$ for different measurement scenarios. For the Tx-cls-LOS scenario, we use the same set of values for large and small scale channel parameters, as used for Fig. 13. Similarly, for the TX-cls-NLOS, Tx-far-LOS and Tx-far-NLOS, we reuse the channel parameters from Fig. 14, Fig. 15 and Fig. 16 respectively. The LLR fusion rule exhibits saturation in the high SINR regime (from 20dB) for NLOS scenario when the SUs are placed far from each other (Fig. 20). Though the LLR rule utilizes more system knowledge (like large and small scale channel statistics, noise and interfering power variance, dependence of output on detection hypothesis etc.) than any other fusion rules, estimate of such system parameters is corrupted with noise, ISI and ICI. Therefore, it is unable to combat residual interference after a certain limit. While on the other hand, the TR-based rules can leverage the channel reciprocity information continuously to improve their performance.

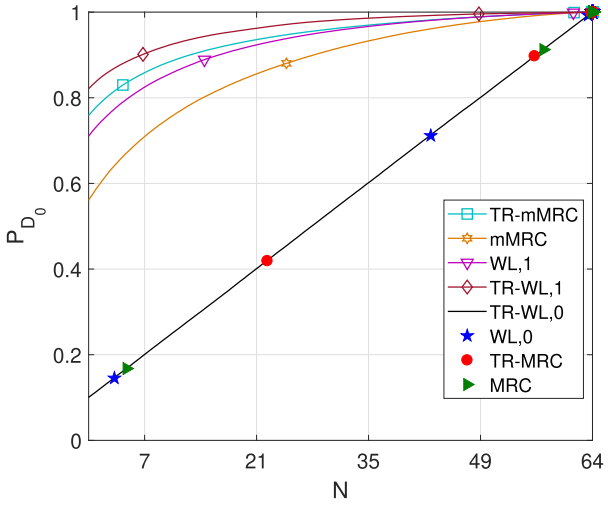

Fig. 21. P_{D_0} v/s N for the case when the SUs are placed close to each other in a LOS scenario.

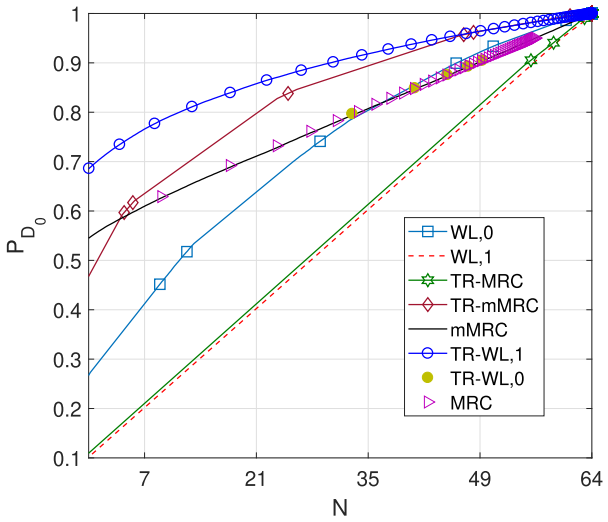

Fig. 22. P_{D_0} v/s N for the case when the SUs are separated by partitions (glass or dry-wall) in a NLOS scenario.

3) P_{D_0} v/s N: In Fig. 21 and Fig. 22, we exhibit probabilities of detection P_{D_0} with two groups of fusion rules (TR and non-TR) as an interpolation function of the number of receive antennas N under $P_{F_0} \leq 0.01$. For both the figures the channel SINR is fixed at 20 dB. The saturation effect that is observed in case of MIMO DF in Wireless Sensor Networks (WSN) [5] is not observed in case of the WSS scenario.

When the SUs are close to each other with a LOS path existing between the SUs and the DFC (refer to Fig. 21), for the case of MRC, TR-MRC, WL,0 and TR-WL,0 rules, P_{D_0} increases proportionally with the increase in N. The mMRC, TR-mMRC, WL,1 and TR-WL,1 rules exploit diversity gain but do not reach saturation for the values of N and the channel SINR considered. However, the increase in P_{D_0} is slower as N increases from 15 to 64 than as N increases from 1 to 15.

When the SUs are far from each other without any LOS path existing between the SUs and the DFC (refer to Fig. 22), for the case of MRC and TR-MRC, as well as WL,1, mMRC and TR-WL,0 rules, P_{D_0} increases proportionally with the increase in N. The TR-WL,1 rule does not reach saturation for

the values of N and the channel SINR considered. However, the increase in P_{D_0} is slower as N increases from 15 to 64 than as N increases from 1 to 15. The increase in P_{D_0} for the WL,0 rule is slowest as N increases from 1 to 15; rate of increase in P_{D_0} increases from 15 to 35 and even more from 35 to 64. The increase in P_{D_0} for the TR-mMRC rule is slowest as N increases from 1 to 7; rate of increase in P_{D_0} increases from 7 to 25 and even more from 25 to 64.

V. Conclusion

The main goal of this paper is to investigate and study the practical implications of employing distributed detection for collaborative WSS in a CR-like network, especially in the light of the recently proposed decision fusion algorithms for DFC equipped with massive number of integrated antennas. The measurement set-up represents a scenario where the SUs compete for frequency bands closely-spaced as in case of multi-carrier systems like OFDM (though in absence of any CP). This is accomplished through a measurement campaign comprising of a 4×64 MIMO set-up using NI USRPs all deployed in an indoor environments. The indoor environments can be static or dynamic (people moving around). Large and small scale channel statistics as well as ISI and ICI corrupting the transmit signal are captured for each measurement scenario and average values of pathloss and shadowing variations are calculated for all cases. Shadowing statistics are observed to follow Gamma distribution and fading statistics are found to be well approximated by Rician distribution with varying K-factors. The channel parameters and interference power encountered in the measured scenarios are directly incorporated in the performance analysis of newly formulated optimal and sub-optimal fusion rules. Results demonstrate that closeness of the SUs benefits performance of all fusion rules. Presence of LOS propagation path also ameliorates performance of sub-optimum rules. The results also demonstrate that mMRC performs better than WL fusion rule in realistic scenario if WL statistics is employed with normal deflection coefficient [4]. If WL statistics is accompanied by modified deflection measure, WL rule outperforms all other rules confirming the observations in [9].

Inspired by the recent success of TR-based methods like TR-MRC and TR-ZF in resolving saturation of SINR owing to residual ISI and ICI, we have proposed TR-MRC, TR-mMRC and TR-WL rules. However, TR-based rules can suffer from restricted performance improvement owing to the limited information available about the environment. In that case, in future, we will resort to space-time spreading of the local SU decisions, before transmission, thereby exploiting multi-slot decisions and even, multi-symbol decisions. If these extensions are incorporated, such a network will benefit from time-integration in sensing performance, opportunistic throughput and interference-free transmission.

References

[1] P. Paysarvi-Hoseini and N. C. Beaulieu, "On the benefits of multi-channel/wideband spectrum sensing with non-uniform channel sensing durations for cognitive radio networks," *IEEE Trans. Commun.*, vol. 60, no. 9, pp. 2434–2443, Sep. 2012.

[2] Z. Quan, S. Cui, A. H. Sayed, and H. V. Poor, "Wideband spectrum sensing in cognitive radio networks," in *Proc. IEEE Int. Conf. Commun.*, 2008, pp. 901–906.

[3] J. Unnikrishnan and V. V. Veeravalli, "Cooperative sensing for primary detection in cognitive radio," *IEEE J. Sel. Topics Signal Process.*, vol. 2, no. 1, pp. 18–27, Feb. 2008.

[4] Z. Quan, S. Cui, and A. H. Sayed, "Optimal linear cooperation for spectrum sensing in cognitive radio networks," *IEEE J. Sel. Topics Signal Process.*, vol. 2, no. 1, pp. 28–40, Feb. 2008.

[5] D. Ciuonzo, G. Romano, and P. S. Rossi, "Channel-aware decision fusion in distributed MIMO wireless sensor networks: Decode-and-fuse vs. Decode-then-fuse," *IEEE Trans. Wireless Commun.*, vol. 11, no. 8, pp. 2976–2985, Aug. 2012.

[6] P. Salvo Rossi, D. Ciuonzo, and G. Romano, "Orthogonality and cooperation in collaborative spectrum sensing through MIMO decision fusion," *IEEE Trans. Wireless Commun.*, vol. 12, no. 11, pp. 5826–5836, Nov. 2013.

[7] I. Dey, M. Majid Butt, and N. Marchetti, "Throughput analysis for virtual MIMO WSNs over measured MIMO channels," *IEEE Trans. Instrum. Meas.*, vol. 68, no. 1, pp. 297–299, Jan. 2019.

[8] I. Dey, P. Salvo Rossi, M. M. Butt, and N. Marchetti, "Virtual MIMO wireless sensor networks: Propagation measurements and fusion performance," *IEEE Trans. Antennas Propag.*, vol. 67, no. 8, pp. 5555–5568, Aug. 2019.

[9] D. Ciuonzo, P. Salvo Rossi, and S. Dey, "Massive MIMO channel-aware decision fusion," *IEEE Trans. Signal Process.*, vol. 63, no. 3, pp. 604–619, Feb. 2015.

[10] G. Ding, X. Gao, Z. Xue, Y. Wu, and Q. Shi, "Massive MIMO for distributed detection with transceiver impairments," *IEEE Trans. Veh. Technol.*, vol. 67, no. 1, pp. 604–617, Jan. 2018.

[11] D. Guimarães, C. da Silva, and R. de Souza, "Cooperative spectrum sensing using eigenvalue fusion for OFDMA and other wideband signals," *J. Sensor Actuator Netw.*, vol. 2, no. 1, pp. 1–24, Jan. 2013.

[12] V. Nsengiyumva, "Is the cyclic prefix needed in massive MIMO?" Division Commun. Syst., Dept. Elect. Eng., Linköping Univ., Linköping, Sweden, Tech. Rep., Jun. 2016.

[13] A. F. Molisch, M. Toeltsch, and S. Vermani, "Iterative methods for cancellation of intercarrier interference in OFDM systems," *IEEE Trans. Veh. Technol.*, vol. 56, no. 4, pp. 2158–2167, Jul. 2007.

[14] J.-B. Lim, C.-H. Choi, and G.-H. Im, "MIMO-OFDM with insufficient cyclic prefix," *IEEE Commun. Lett.*, vol. 10, no. 5, pp. 356–358, May 2006.

[15] Z. Chen, C. Yongyu, and D. Yang, "Low-complexity turbo equalization for MIMO-OFDM system without cyclic prefix," in *Proc. IEEE 20th Int. Symp. Pers., Indoor Mobile Radio Commun.*, Sep. 2009, pp. 310–314.

[16] S. Ma and T.-S. Ng, "Two-step signal detection for MIMO-OFDM systems without cyclic prefix," in *Proc. IEEE Wireless Commun. Netw. Conf.*, Apr. 2009, pp. 1–6.

[17] B. Chen, R. Jiang, T. Kasetkasem, and P. K. Varshney, "Channel aware decision fusion in wireless sensor networks," *IEEE Trans. Signal Process.*, vol. 52, no. 12, pp. 3454–3458, Dec. 2004.

[18] W. Li and H. Dai, "Distributed detection in wireless sensor networks using a multiple access channel," *IEEE Trans. Signal Process.*, vol. 55, no. 3, pp. 822–833, Mar. 2007.

[19] K. Patil, R. Prasad, and K. Skouby, "A survey of worldwide spectrum occupancy measurement campaigns for cognitive radio," in *Proc. Int. Conf. Devices Commun. (ICDeCom)*, Feb. 2011, pp. 1–5.

[20] Y. Chen and H.-S. Oh, "A survey of measurement-based spectrum occupancy modeling for cognitive radios," *IEEE Commun. Surveys Tuts.*, vol. 18, no. 1, pp. 848–859, 1st Quart., 2016.

[21] S. Subramaniam, H. Reyes, and N. Kaabouch, "Spectrum occupancy measurement: An autocorrelation based scanning technique using USRP," in *Proc. IEEE 16th Annu. Wireless Microw. Technol. Conf. (WAMICON)*, Apr. 2015, pp. 1–5.

[22] P. Harris *et al.*, "LOS throughput measurements in real-time with a 128-antenna massive MIMO testbed," in *Proc. IEEE Global Commun. Conf. (GLOBECOM)*, Dec. 2016, pp. 1–7.

[23] X. Gao, O. Edfors, F. Rusek, and F. Tufvesson, "Massive MIMO performance evaluation based on measured propagation data," *IEEE Trans. Wireless Commun.*, vol. 14, no. 7, pp. 3899–3911, Jul. 2015.

[24] P. Harris *et al.*, "Performance characterization of a real-time massive MIMO system with LOS mobile channels," *IEEE J. Sel. Areas Commun.*, vol. 35, no. 6, pp. 1244–1253, Jun. 2017.

[25] J. Flordelis, X. Gao, G. Dahman, F. Rusek, O. Edfors, and F. Tufvesson, "Spatial separation of closely-spaced users in measured massive multi-user MIMO channels," in *Proc. IEEE Int. Conf. Commun. (ICC)*, Jun. 2015, pp. 1441–1446.

[26] J. Li *et al.*, "Measurement-based characterizations of indoor massive MIMO channels at 2 GHz, 4 GHz, and 6 GHz frequency bands," in *Proc. IEEE 83rd Veh. Technol. Conf. (VTC Spring)*, May 2016, pp. 1–5.
[27] S. Payami and F. Tufvesson, "Delay spread properties in a measured massive MIMO system at 2.6 GHz," in *Proc. IEEE 24th Annu. Int. Symp. Pers., Indoor, Mobile Radio Commun. (PIMRC)*, Sep. 2013, pp. 53–57.
[28] B. Ai *et al.*, "On indoor millimeter wave massive MIMO channels: Measurement and simulation," *IEEE J. Sel. Areas Commun.*, vol. 35, no. 7, pp. 1678–1690, Jul. 2017.
[29] A. O. Martinez, J. O. Nielsen, E. De Carvalho, and P. Popovski, "An experimental study of massive MIMO properties in 5G scenarios," *IEEE Trans. Antennas Propag.*, vol. 66, no. 12, pp. 7206–7215, Dec. 2018.
[30] V. Kristem *et al.*, "3D MIMO outdoor-to-indoor propagation channel measurement," *IEEE Trans. Wireless Commun.*, vol. 16, no. 7, pp. 4600–4613, Jul. 2017.
[31] S. Sangodoyin *et al.*, "Cluster characterization of 3-D MIMO propagation channel in an urban macrocellular environment," *IEEE Trans. Wireless Commun.*, vol. 17, no. 8, pp. 5076–5091, Aug. 2018.
[32] A. Aminjavaheri, A. Farhang, A. Rezazadehreyhani, L. E. Doyle, and B. Farhang-Boroujeny, "OFDM without CP in massive MIMO," *IEEE Trans. Wireless Commun.*, vol. 16, no. 11, pp. 7619–7633, Nov. 2017.
[33] P. K. Sangdeh, H. Pirayesh, H. Zeng, and H. Li, "A practical underlay spectrum sharing scheme for cognitive radio networks," in *Proc. IEEE Conf. Comput. Commun. (INFOCOM)*, Apr. 2019, pp. 2521–2529.
[34] T. S. Rappaport, S. Y. Seidel, and K. Takamizawa, "Statistical channel impulse response models for factory and open plan building radio communicate system design," *IEEE Trans. Commun.*, vol. 39, no. 5, pp. 794–807, May 1991.
[35] W. C. Navidi, *Statistics for Engineers and Scientists*. 1st ed. New York, NY, USA: McGraw-Hill, 2006.
[36] L. J. Greenstein, D. G. Michelson, and V. Erceg, "Moment-method estimation of the Ricean K-factor," *IEEE Commun. Lett.*, vol. 3, no. 6, pp. 175–176, Jun. 1999.
[37] Y. Bar-Shalom, T. Kirubarajan, and X. R. Li, *Estimation With Applications to Tracking and Navigation: Theory Algorithms and Software*. Hoboken, NJ, USA: Wiley, 2004.

I. Dey (Member, IEEE) received the M.Sc. degree in wireless communications from the University of Southampton, Southampton, U.K., in 2010, and the Ph.D. degree in electrical engineering from the University of Calgary, Calgary, Canada, in 2015. From 2015 to 2016, she was a Post-Doctoral Research Fellow with the Ultra-Maritime Digital Communication Center, Dalhousie University, Canada. She was a Research Fellow with the Department of Electronics and Telecommunications, Norwegian University of Science and Technology, Trondheim, Norway, from 2016 to 2017. From 2017 to 2019, she was a Marie Skłodowska-Curie (EDGE) Fellow with the Trinity College Dublin, Ireland. She is currently a Lecturer/Assistant Professor with the Department of Electronic Engineering, National University of Ireland, Maynooth. She conducts her research at the Irish Research Centre for Future Networks and Communications (CONNECT). Her current research interests include channel modeling, channel estimation and prediction, adaptive modulation, and dirty tape coding for different wireless propagation environments, and wireless sensor networks. In 2016, she received the prestigious Alain Bensoussan Research Fellowship from the European Research Consortium for Information and Mathematics (ERCIM).

P. Salvo Rossi (Senior Member, IEEE) was born in Naples, Italy, in April 1977. He received the Dr.Eng. degree in telecommunications engineering *(summa cum laude)* and the Ph.D. degree in computer engineering from the University of Naples "Federico II", Italy, in 2002 and 2005, respectively. From 2005 to 2008, he has worked as a Post-Doctoral Researcher with the Department of Computer Science and Systems, University of Naples "Federico II", the Department of Information Engineering, Second University of Naples, Italy, and the Department of Electronics and Telecommunications, Norwegian University of Science and Technology (NTNU), Norway. From 2008 to 2014, he was an Assistant Professor (tenured in 2011) in telecommunications with the Department of Industrial and Information Engineering, Second University of Naples. From 2014 to 2016, he was an Associate Professor in signal processing with the Department of Electronics and Telecommunications, NTNU. From 2016 to 2017, he was a Full Professor in signal processing with the Department of Electronic Systems, NTNU. From 2017 to 2019, he was a Principal Engineer with the Department of Advanced Analytics and Machine Learning, Kongsberg Digital AS, Norway. He held visiting appointments at the Department of Electrical and Computer Engineering, Drexel University, USA, the Department of Electrical and Information Technology, Lund University, Sweden, the Department of Electronics and Telecommunications, NTNU, and the Excellence Center for Wireless Sensor Networks, Uppsala University, Sweden. Since 2019, he has been a Full Professor in statistical machine learning with the Department of Electronic Systems, NTNU, where he is also the Director of IoT@NTNU. His research interests fall within the areas of communication theory, data fusion, machine learning, and signal processing. He was awarded as an Exemplary Senior Editor for IEEE COMMUNICATIONS LETTERS in 2018. He was an Associate Editor and a Senior Editor for IEEE COMMUNICATION LETTERS from 2012 to 2016 and 2016 to 2019, respectively. He has been serving as an Executive Editor for IEEE COMMUNICATION LETTERS since 2019, an Area Editor for IEEE OPEN JOURNAL OF THE COMMUNICATIONS SOCIETY since 2019, an Associate Editor for IEEE TRANSACTIONS ON SIGNAL AND INFORMATION PROCESSING OVER NETWORKS since 2019, and an Associate Editor for IEEE TRANSACTIONS ON WIRELESS COMMUNICATION since 2015.

M. Majid Butt (Senior Member, IEEE) received the M.Sc. degree in digital communications from Christian Albrechts University, Kiel, Germany, in 2005, and the Ph.D. degree in telecommunications from the Norwegian University of Science and Technology, Trondheim, Norway, in 2011. He is currently a Senior Scientist 5G+ Research at Nokia Bell Labs, France, and a Visiting Research Assistant Professor with the Trinity College Dublin, Ireland. Before that, he has held various positions at the University of Glasgow, U.K., the Trinity College Dublin, Ireland, Fraunhofer HHI, Germany, and the University of Luxembourg. His major areas of research interest include communication techniques for wireless networks with a focus on radio resource allocation, scheduling algorithms, energy efficiency, and machine learning for RAN. He has authored more than 60 peer reviewed conference and journal publications in these areas. He was a recipient of the Marie Curie Alain Bensoussan Postdoctoral Fellowship from European Research Consortium for Informatics and Mathematics (ERCIM). He has served as the organizer/chair for various technical workshops on various aspects of communication systems in conjunction with major IEEE conferences, including WCNC, Globecom, and Greencom. He has been serving as an Associate Editor for IEEE ACCESS journal and *IEEE Communication Magazine* since 2016.

Nicola Marchetti (Senior Member, IEEE) received the Ph.D. degree in wireless communications from Aalborg University, Denmark, in 2007, the M.Sc. degree in electronic engineering from the University of Ferrara, Italy, in 2003, and the M.Sc. degree in mathematics from Aalborg University in 2010. He performs his research under the Irish Research Centre for Future Networks and Communications (CONNECT), where he leads the Wireless Engineering and Complexity Science (WhyCOM) Lab. He is currently an Associate Professor in wireless communications at Trinity College Dublin, Ireland. He has authored in excess of 140 journals and conference papers, two books and eight book chapters, holds four patents, and received four best paper awards. His research interests include radio resource management, self-organizing networks, complex systems science, and signal processing for communication networks. He serves as an Associate Editor for the IEEE INTERNET OF THINGS Journal since 2018, and the *EURASIP Journal on Wireless Communications and Networking* since 2017.